

Article

Geology, Pyrite Geochemistry and Metallogenic Mechanism of the Wulong Gold Deposit in Liaodong Peninsula, North China Craton

Zhichao Zhang ^{1,*}, Yuwang Wang ¹, Jiyu He ², Dedong Li ¹, Haicheng Qiu ³, Fuxing Liu ⁴ and Chunkit Lai ⁵

¹ Deep Exploration Technic Center for Non-Ferrous Mines, Beijing Institute of Geology for Mineral Resources Co., Ltd., Beijing 100012, China

² Sino-Zijin Resources Ltd., Beijing 100012, China

³ Liaoning Wulong Gold Mining Co., Ltd., Dandong 118012, China

⁴ 103 Branch of Non-Ferrous Geological of Liaoning Province Co., Ltd., Dandong 118008, China

⁵ Faculty of Science, University Brunei Darussalam, Gadong BE1410, Brunei

* Correspondence: zzc_cugb@126.com

Abstract: The Wulong deposit is a large gold deposit in the Liaodong peninsula (North China Craton). Silicic and pyrite alterations are well-developed in the deposit and closely related to mineralization. The least altered and silicified microdiorite samples were selected for major and trace element analyses to reveal the elemental migration/enrichment. Pyrites of stage 1 (Py1) were selected for backscattered electron (BSE) imaging and LA-ICP-MS trace element analyses to reveal their possible metallogenic link. Mass balance calculation showed that Al₂O₃, CaO, Fe₂O₃, K₂O, SiO₂, Ag, As, Cu, and Pb were brought in, whereas MgO, Na₂O, FeO, Cr, Zn, and Ni were leached out during silicification. LA-ICP-MS trace element analyses show that Py1 has higher Au and Zn contents than Py2 and Py3, Py2 has higher Au and Cu contents than Py1 and Py3, and Py3 has higher Pb, Cu, and As contents than Py1 and Py2. During the process of silicification and pyritization, the depleted H⁺ concentration and HS[−] concentration in the ore-forming fluids led to instability of the Au(HS)^{2−} complexes and led to gold precipitation. The depleted sulfur and the reduced temperature during the precipitated of bismuthinite also led to instability of the Au(HS)^{2−} complexes and gold precipitation.

Keywords: mass balance; trace elements; mineralization mechanism; Wulong gold deposit; North China Craton



Citation: Zhang, Z.; Wang, Y.; He, J.; Li, D.; Qiu, H.; Liu, F.; Lai, C. Geology, Pyrite Geochemistry and Metallogenic Mechanism of the Wulong Gold Deposit in Liaodong Peninsula, North China Craton. *Minerals* **2022**, *12*, 1551. <https://doi.org/10.3390/min12121551>

Academic Editors:
Callum Hetherington and
Kunfeng Qiu

Received: 9 October 2022
Accepted: 28 November 2022
Published: 30 November 2022

Publisher's Note: MDPI stays neutral with regard to jurisdictional claims in published maps and institutional affiliations.



Copyright: © 2022 by the authors. Licensee MDPI, Basel, Switzerland. This article is an open access article distributed under the terms and conditions of the Creative Commons Attribution (CC BY) license (<https://creativecommons.org/licenses/by/4.0/>).

1. Introduction

The Liaodong region (North China Craton) is a major gold province in NE Asia [1–8]. Gold deposits are mainly distributed in Qingchengzi, Wulong, and Maoling ore concentration areas, which formed during the Early Cretaceous. The Wulong ore concentration area has a long history of mining and is an important Au metallogenic area [9]. The Wulong deposit is a large gold deposit in the Wulong ore concentration area [10]. The Wulong gold deposit is related to high-angle strike-slip faults [11]. More than 80 tons of gold have been identified at an average grade of 5.35 g/t since the deposit was discovered in 1939 [12]. Alteration is well-developed in the mining area, including silicification, pyritization, sericitization, chloritization, and carbonatization, among which the former two are closely mineralization-related [10,12–14]. Pyrite is the main gold-bearing mineral in the Wulong deposit. Bismuthinite is often associated with gold. Native gold is often found in or around bismuthinite. The other gold deposits in the Liaodong region do not contain bismuthinite [10,12–14].

During hydrothermal fluid–rock reactions, elemental migration/enrichment can change the physicochemical conditions of hydrothermal fluids, which could destabilize gold-bisulfide complexes and cause gold precipitation [9–21]. Thus, the study of elemental migration/enrichment can reveal ionic substitution reactions, ore-fluid compositions, as well as

the mechanism of alteration and gold precipitation [22–30]. Silicification and pyritization are important prospecting indicators at Wulong. Reference [14] suggested that the major elements (SiO_2 , K_2O , P_2O_5 , and Fe_2O_3) are brought into the alteration system, and that contents of certain trace elements (V, Y, Zr, Ni, Co, and Sr) increase and decrease in the altered granite and diorite dike, respectively. Nonetheless, the elemental migration/enrichment and metallogenic implications of the silicification at Wulong are yet to be clear. The genetic relationship between silicification and gold precipitation is unclear as well.

Pyrite is a common component of ore-bearing mineral assemblages and can provide valuable information regarding ore-forming processes. Thus, LA-ICP-MS trace element analysis of pyrite can provide some information on the processes of gold deposition and evolution [18,22]. Ref. [12] studied the pyrite generation and trace element distribution of pyrite from different mineralization stages of the Wulong deposit, which suggested that gold concentrations in Py2 are higher than those in Py1 and Py3, and gold mineralization occurred primarily during the middle stage. High Co/Ni ratios of pyrite are consistent with a hydrothermal origin. However, the gold precipitation mechanism and ore-forming processes of the Wulong deposit are yet to be clear.

Based on detailed field macroscopic and thin-section microscopic observations, this study explores the spatial–temporal relationship between alteration and mineralization. To reveal the elemental migration/enrichment, alteration–mineralization relationships, and gold precipitation mechanism, we conducted backscattered electron (BSE) imaging and LA-ICP-MS trace element analysis on pyrite from stage 1 and mass balance calculation of the silicification process.

2. Geological Setting

The Liaodong Peninsula is located in the eastern margin of the North China Craton (Figure 1a), bounded by the Yalujiang fault in the east and the Tanlu fault in the west [2,31]. The Liaodong Peninsula has experienced multistage Paleoproterozoic tectonism and metamorphism [32–34]. The current tectonic framework of the Liaodong Peninsula was mainly formed in the Mesozoic post-collision extensional setting [35,36]. The Liaodong Peninsula was in a post-collisional extension tectonic setting during the Triassic period. The North China Craton in the north was subducted by the Paleo-Pacific plate in the south. The subduction between the Paleo-Pacific plate and North China Cratons led to the thickening of lithosphere during the Jurassic period. Large-scale delamination took place in the Cretaceous period. In addition, the Wulong gold deposit was formed at this time [32].

The geology of the Wulong orefield is composed mainly of the Paleoproterozoic Liaohé Group, which includes the Yujiapuzi, Langzishan, Dashiqiao, and Gaixian Formations, the Sinan Diaoyutai Formation, and the Jurassic Xiaotonggou Formation (Figure 1b) [37,38]. The Yujiapuzi and Langzishan Formations are composed of marble, hornblende schist, and biotite schist [12]. The Dashiqiao Formation contains marble, and minor mica schist, and carbonaceous slate. The Gaixian Formation is composed of mica schist, leptynite, slate, and phyllite [10,39]. The Diaoyutai Formation is composed of sandstone, quartzite, and breccia. The Xiaotonggou Formation is composed of volcanic–volcaniclastic rocks [10].

The NE-trending Yalujiang fault, a first-order structure in the region, is characterized by multistage activities [40,41]. In the orefield, a series of approximately NNE-trending second-order faults (e.g., Zhengjiapu, Heigou, Jixingou, Yangjia, and Hongshi) are developed on the western side of the Yalujiang fault (Figure 1b) [12,42]. These faults are kilometers long and several meters to 40 m wide, and dip to the NW with dip angles of 40° – 60° [43]. Massive fault gouges as well as lenses of microdiorite and auriferous quartz veins are developed within the faults, recording various stages of deformation [42]. The Jixinling fault is the closest to the Wulong deposit and is a major ore-bearing structure [12].

Intrusive rocks in the region are dominantly Yanshanian gneissic two-mica granite, granodiorite, and porphyritic granite (Figure 1b). The gneissic two-mica granite was zircon U–Pb dated to be 163 ± 7 Ma [36]. The granodiorite (at Sanguliu) and porphyritic granite (at Dingqishan and Wulongbei) were zircon U–Pb dated to be 129.0 ± 2.9 Ma [38] and

127 ± 5 Ma [12,44], respectively. The gneissic two-mica granite and diorite are important ore-bearing wallrocks, and thus the Yanshanian magmatism is commonly regarded to be genetically linked to the Wulong gold mineralization [45,46].

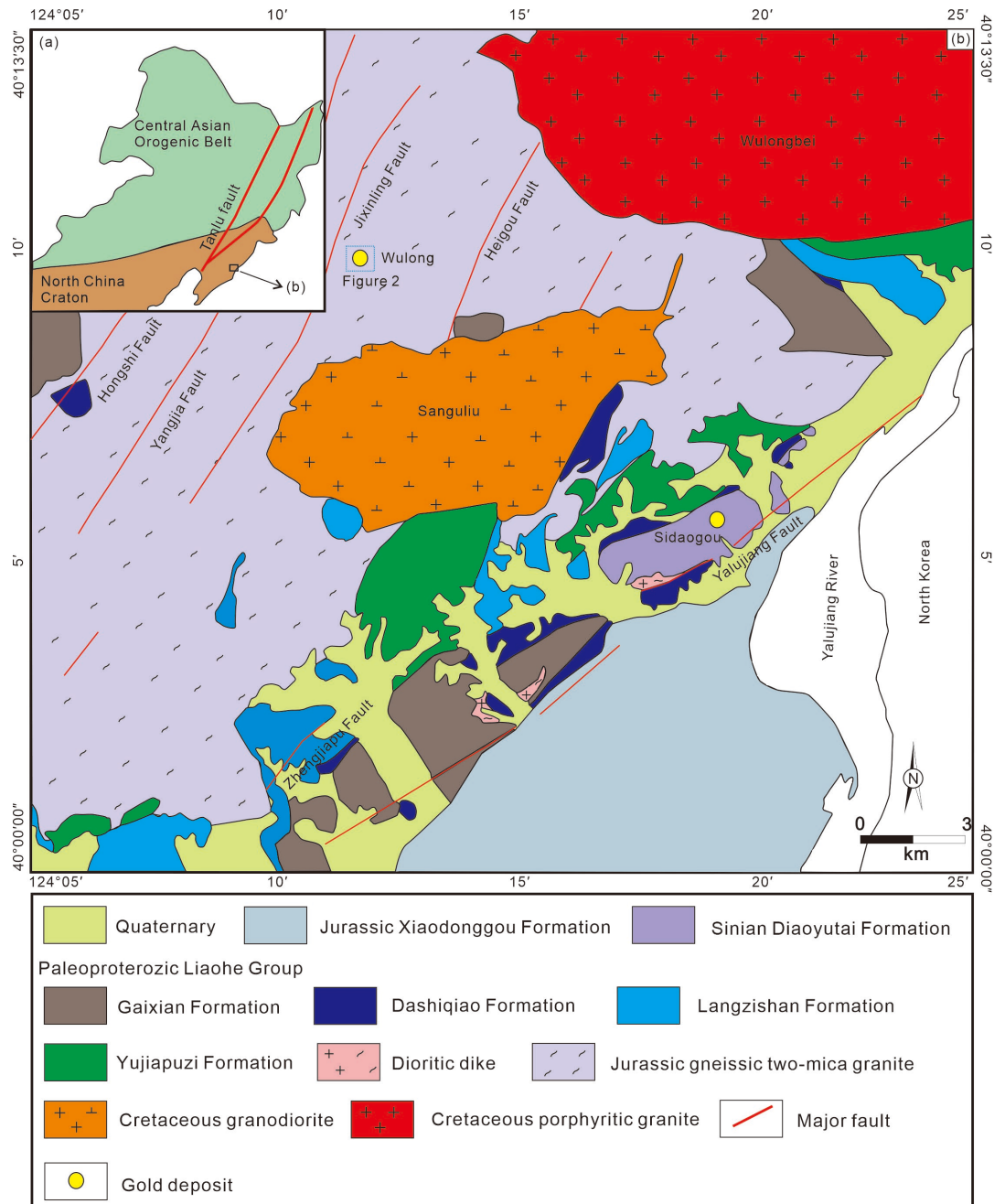


Figure 1. Simplified tectonic maps of (a) Liaodong Peninsula, showing the major faults and tectonic blocks; (b) Regional geologic map of the Wulong orefield. Modified from [12].

3. Deposit Geology

The Wulong deposit is located in the northwestern Wulong orefield (Figure 1b) and contains more than 80 metric tons of Au with an average grade of 5.35 g/t [47]. Exposed sequences at Wulong comprise the Paleoproterozoic Dashiqiao Formation marble, the Gaixian Formation mica schist, leptynite, slate, and phyllite, as well as Quaternary sediments [10].

Faults (EW-, NE-/NNE-, NS-, and NW-trending) are common at the Wulong deposit and can be divided into pre-ore, syn-ore, and post-ore faults [10,13]. Pre-ore faults include EW-trending compressional and NS-trending extensional ones. EW-trending faults dip

to the SE with dip angles of 50° ~ 70° and are intruded by microdiorite and quartz veins. NS-trending faults are largely vertical and intruded by granitic porphyry [10,12]. Syn-ore faults include NNE-trending transpressional and NW-trending transtensional faults. NNE-trending faults dip to the west with dip angles of 75° ~ 85° , whilst NW-trending faults dip to the SW with dip angles of 50° ~ 70° . Both NNE- and NW-trending faults are secondary structures of the Jixinling fault and are intruded by microdiorite and auriferous quartz veins (thus ore-bearing) (Figure 2). Post-ore faults are NE-trending compressional dips to NW with dip angles of 30° ~ 50° [10,12,32].

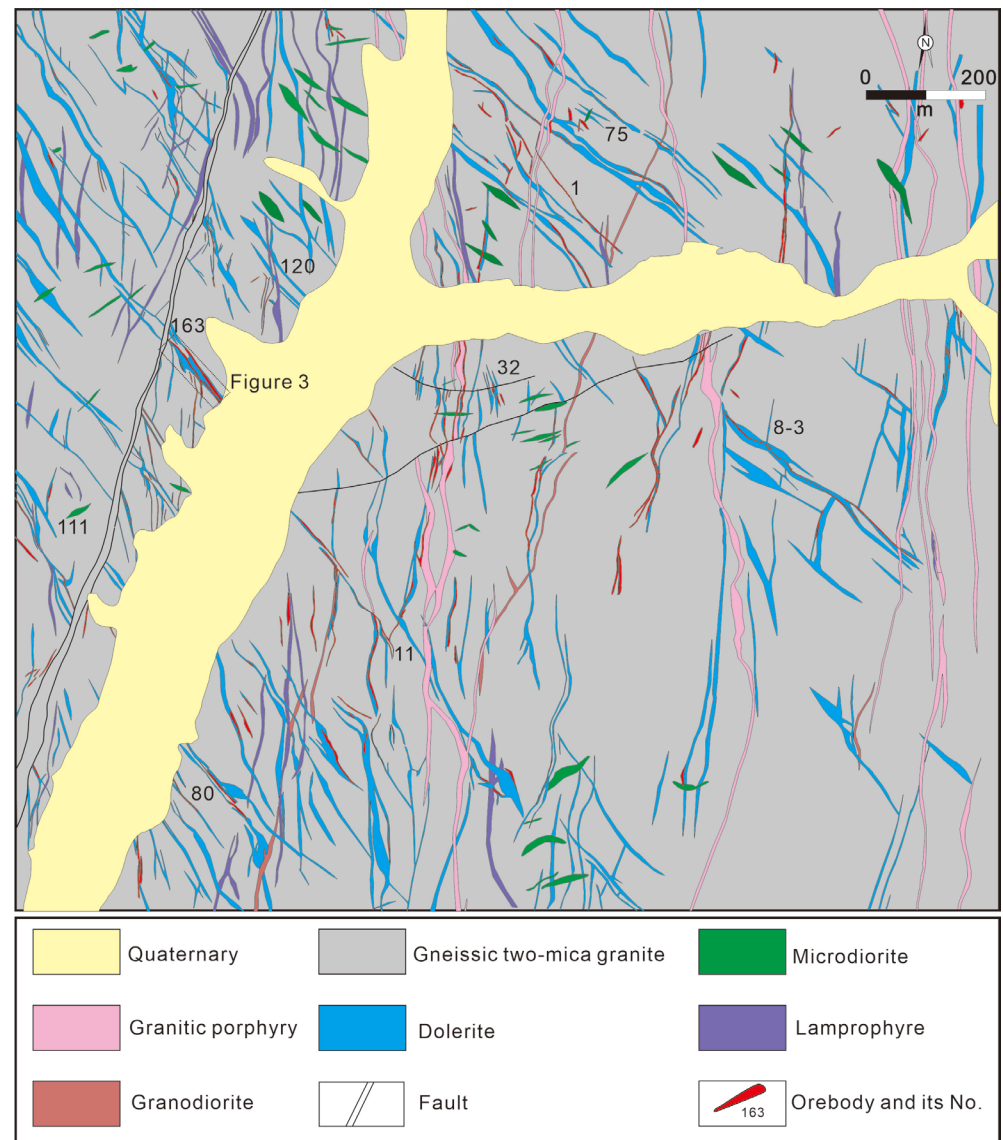


Figure 2. Simplified geologic map of the Wulong gold deposit showing the distribution of major host rocks, orebodies, and alteration zones. Modified from [10].

Late Jurassic pre-ore gneissic two-mica granite and Early Cretaceous microdiorite, granitic porphyry, and post-ore lamprophyre and dolerite dikes are widely developed at the Wulong deposit [32]. The microdiorite dikes are important ore-host rocks and their emplacement is controlled by NNE- and NW-trending faults, in which auriferous quartz veins are developed. The NS-trending granitic porphyry and granodiorite dikes crosscut the microdiorite and were thus formed after the latter. The post-ore NS-trending lamprophyre and EW-trending dolerite dikes are also younger than the microdiorite and are tens of meters long and 1 to 2 m wide [10,12,32]. Gneissic two-mica granite contains

quartz, feldspar, muscovite, and biotite. The quartz and feldspar are lineated in the gneissic two-mica granite. Microdiorite contains plagioclase, amphibole, biotite, and quartz. Gold-bearing quartz veins often distribute along and in the edges of microdiorite dikes. Granitic porphyry contains quartz, plagioclase, potassium feldspar, biotite, and amphibole. The number of granite porphyry dikes is less than microdiorite dikes. Lamprophyre dikes and dolerite dikes cut off orebodies.

There are over 380 auriferous quartz veins at the Wulong deposit. The orebodies strike NNE, NW and are controlled by faults. Major orebodies include V₁, V₈₋₃, V₁₁, V₃₂, V₇₅, V₈₀, V₁₁₁, V₁₂₀, and V₁₆₃ [10]. The orebodies appear veined and have the characteristic of balk reappear, compound of branch along the trend of the orebody extension. The orebody V₁₆₃ and the orebody V₃₂ are the largest orebodies in the mining area. The orebody V₁₆₃ is auriferous quartz vein type, which strikes NW and dips SW at 70°~80° and is about 430 m long and 0.3 to 2.5 m wide. The Au grade ranges from 0.60 to 53.90 g/t (average 8.09 g/t). The orebody V₃₂ is auriferous quartz vein type, which strikes NNE and dips toward E at 60°~80° and is about 352 m long and 0.6 to 5.36 m wide. The Au grade ranges from 1.51 to 7.87 g/t (average 3.71 g/t). For both orebodies V₁₆₃ and V₃₂, the hanging wall and footwall of the orebody comprise gneissic two-mica granite and microdiorite, respectively (Figure 3) [12,32].

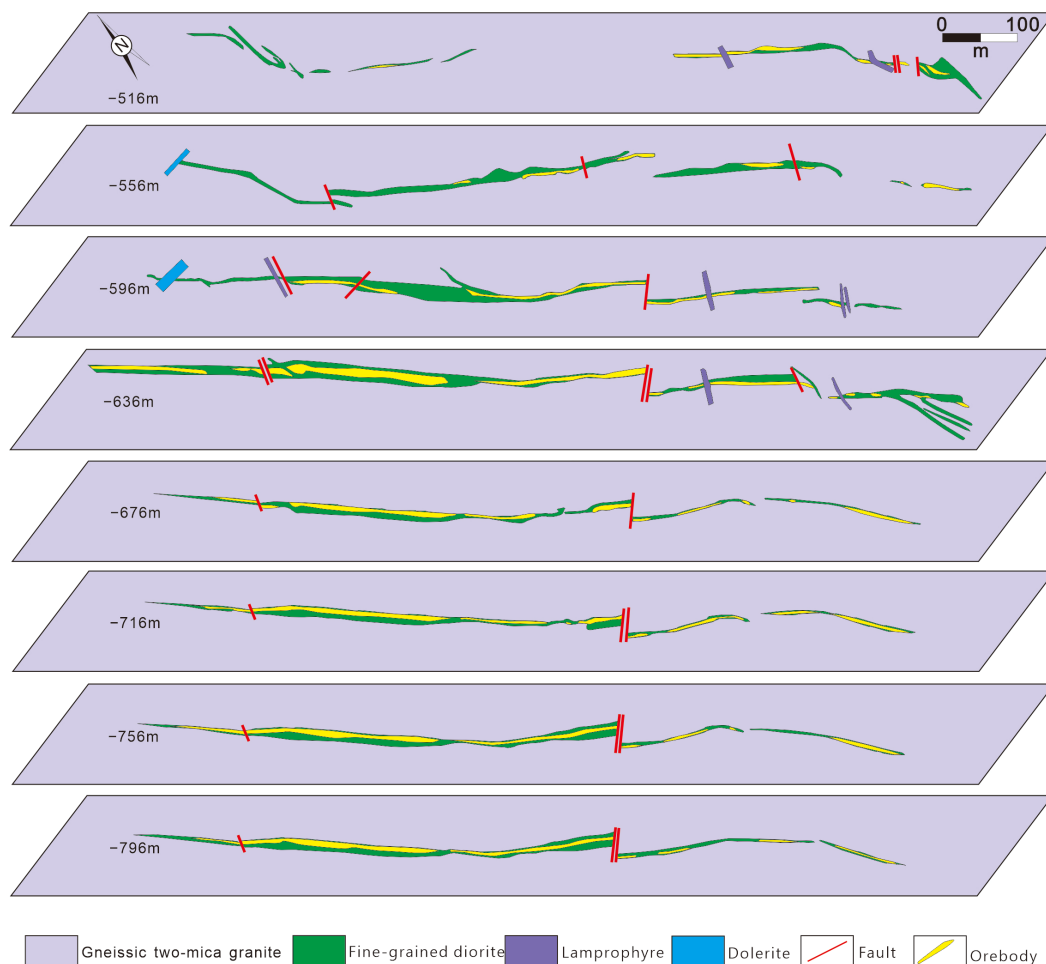


Figure 3. Geologic map of the V163 vein at different levels in the Wulong gold deposit. Modified from [12].

Mineralization at Wulong can be divided into three stages [38,42,45]: (1) quartz-pyrite, (2) quartz-polymetallic sulfide, and (3) quartz-calcite. Stage 1 and stage 2 are the main ore stage. Stage 1 metallic mineral assemblage comprises native gold (Figure 4a), pyrite (Figure 4a,b), bismuthinite (Figure 4c), galena, and sphalerite, whilst that of stage 2

comprises pyrite, bismuthinite, galena, sphalerite, chalcocopyrite, and pyrrhotite. Abundant native gold is observed in this stage (Figure 4b). Pyrite, quartz, calcite, sericite, and chlorite are formed at stage 3 [10,12,13]. Pyrite is the main gold-bearing mineral. Pyrite of stage 1 (Py1) occurs as subhedral grains and ranges from tens to thousands of μm (Figure 4d,e). The content of pyrite in ore ranges from 1% to 10%. Pyrite in ore often shows stellate distributed, disseminated, veined, and occurs with bismuthinite, galena, and sphalerite. Micron-size native gold inclusions are present in Py1. Pyrite of stage 2 (Py2) occurs as subhedral grains and ranges from tens to thousands of μm (Figure 4f,g). The content of pyrite in ore ranges from 1% to 5%. Pyrite in ore often shows stellate distributed, disseminated, and occurring with galena, sphalerite, and chalcocopyrite. Py2 is formed in the middle-stage veins and most Py2 is surrounded by quartz; moreover, some are overprinted by late-stage calcite veins. Micron-size native gold inclusions are present in Py2. Pyrite of stage 3 (Py3) occurs as subhedral grains and ranges from tens to thousands of μm (Figure 4h,i). The content of pyrite in ore ranges from 0.1% to 1%. Pyrite in ore often shows stellate distributed, disseminated, and occurring with calcite, sericite, and chlorite. Py3 is formed in the quartz-calcite veins.

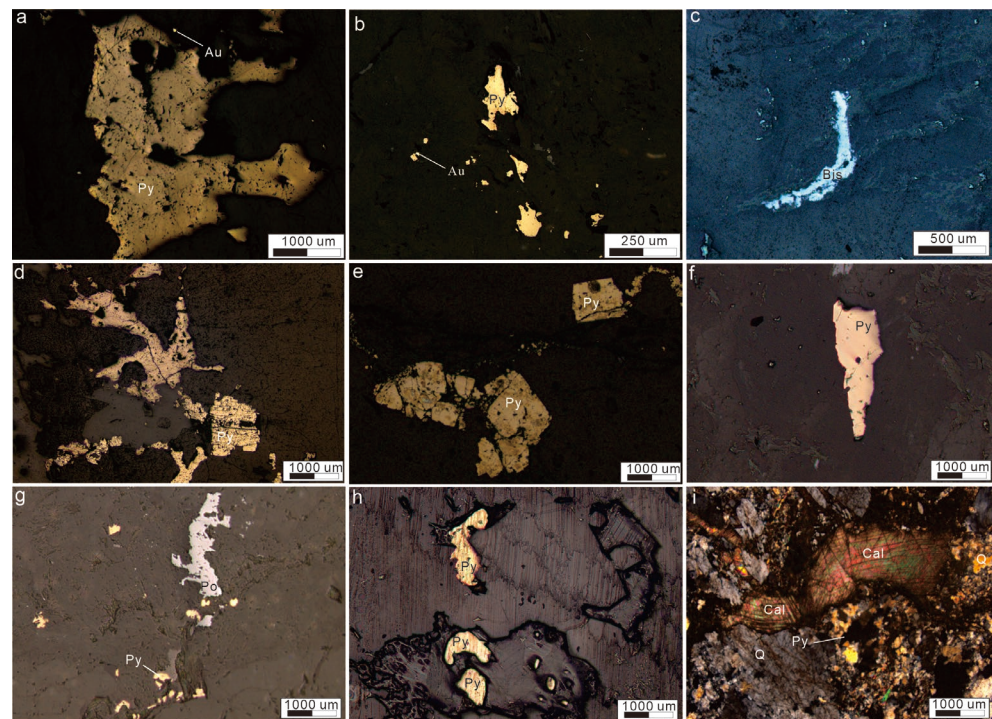


Figure 4. Photomicrographs showing the textural characteristics of pyrite and its relationships with native gold and other sulfides. (a) The textural characteristics of native gold and Py2; (b) The textural characteristics of native gold and Py2; (c) The textural characteristics of bismuthinite; (d) The textural characteristics of Py1; (e) The textural characteristics of Py1; (f) The textural characteristics of Py2; (g) The textural characteristics of Py2 and pyrrhotite; (h) The textural characteristics of Py3; (i) The textural characteristics of Py3, quartz, and calcite. Abbreviations: Py—pyrite; Au—gold; Bis—bismuthinite; Po—pyrrhotite; Qtz—quartz; Cal—calcite.

Hydrothermal alteration is well-developed at Wulong, including mainly silicic, pyrite, sericite, chlorite, and carbonate alterations, in which the former two are closely ore-related [10,12,13]. Silicification and pyritization alteration are spatially and temporally associated with high-grade gold mineralization and occur outside of the orebody. Silicification is characterized by abundant quartz veins associated with pyrite and sericite alterations. The intensity of silicification gradually decreases outward from the orebody (Figure 5). Pyrite is the main gold-bearing mineral, and pyritization also fades away from the orebody

like silicification (Figure 5). Pyritization near the orebody is characterized by abundant quartz associated with sericite, muscovite, and pyrite. Sericitization occurs around the orebody and outside of the silicification zone and occurs with quartz and pyrite to form pyritic-phyllic alterations. Chloritization is orebody distal and is not ore-related [10,12,13]. Chloritization occurs in the outermost zone and is typically dominated by assemblages of chlorite, epidote, quartz, sericite, and calcite. Carbonatization is widespread with euhedral to subhedral carbonate minerals occurring in veins and veinlets.

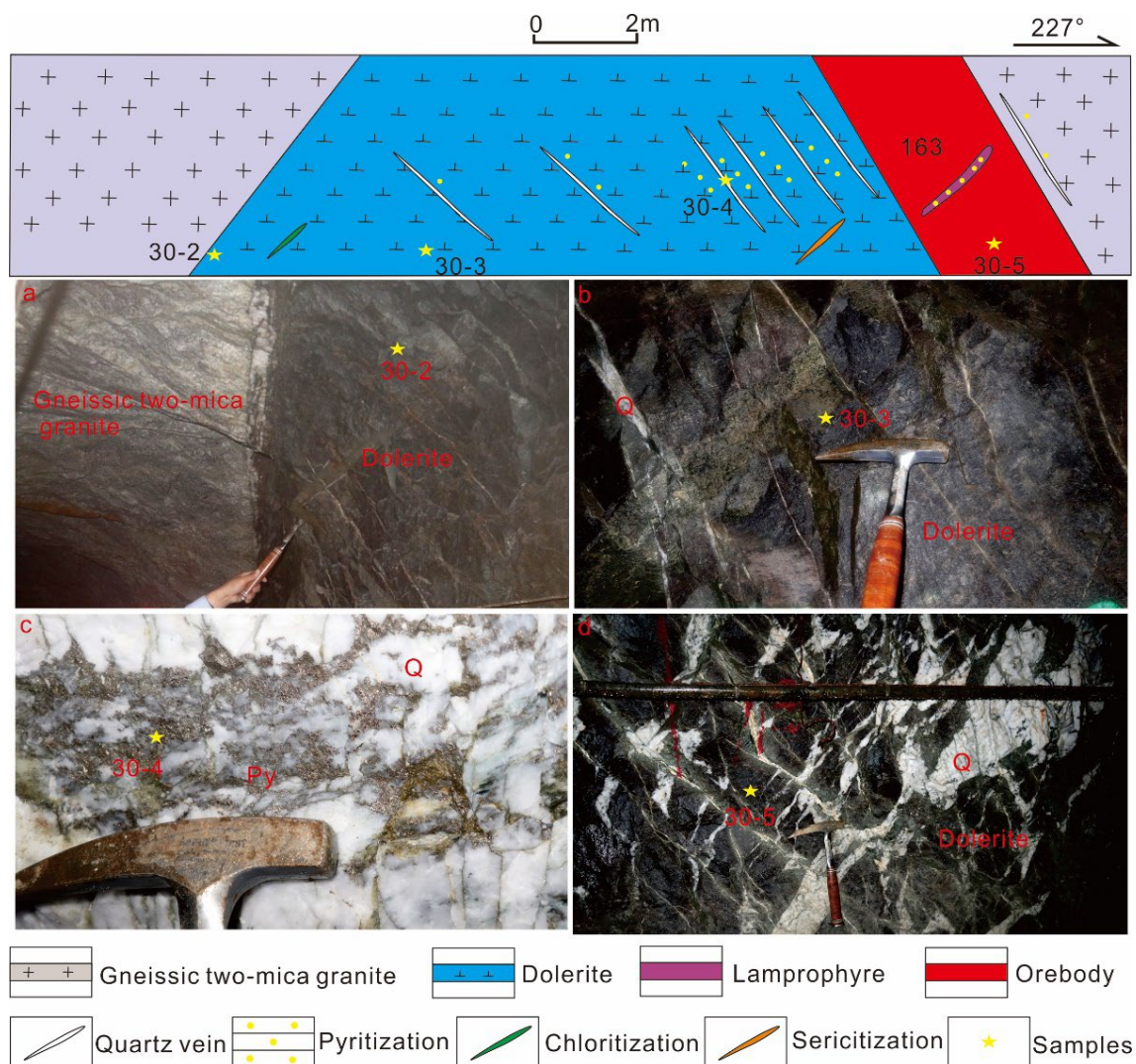


Figure 5. Spatial alteration features in a typical field profile of underground tunnels at -756 m level. (a) The boundary between gneissic two-mica granite and dolerite; (b) The intensity of silicification is weak in diorite; (c) Pyrite in ore; (d) The intensity of silicification is strong in diorite. Abbreviations: Py—pyrite; Q—quartz.

4. Sampling and Analytical Methods

In this study, the least altered and silicified microdiorite samples were selected for whole-rock major and trace element analyses. Moreover, pyrite of stage 1 (Py1) was selected for backscattered electron (BSE) imaging and LA-ICP-MS trace element analyses. Due to the restriction of mining conditions, samples of Py2 and Py3 were not collected in this study. The trace element dates of Py2 and Py3 were collected from [12]. The least altered ($n = 8$) and silicified ($n = 4$) microdiorite samples were collected from underground tunnels at the -756 m level (Figure 5). Pyrite samples ($n = 26$) from the silicified microdiorite samples were also collected from underground tunnels at the -756 m level.

Major and trace element concentrations were analyzed at ALS Minerals (Guangzhou). Major element contents were measured with an XRF-1500 X-ray fluorescence spectrometer using fused glass disks, with analytical precision better than 1%. Trace element concentrations were analyzed by solution ICP-MS after acid digestion of the samples, with precision better than 5%.

The petrological features of sandstones and mineralogical characteristics of pyrite micromorphologies were characterized by secondary electron (SE) and backscattered electron (BSE) imaging using a Zeiss ULTRA PLUS scanning electron microscope (SEM) equipped with Oxford IE350 X-MAX20 electric refrigeration energy spectrometer at the National Research Center for Geoanalysis, China Geological Survey. Operating conditions for the SEM were 15 kV accelerating voltage and the maximum magnification was 1,000,000 times. A high energy electron beam was generated through a scanning electron microscope filament and applied to the surface of the sample. A total of 99% of the energy of the incident electron beam is converted into thermal energy dissipation, and about 1% of the electron energy is excited from the sample, such as secondary electrons, backscattered electrons, characteristic X-rays, Auger electrons, transmission electrons, etc., which are received by the probe to obtain the morphology, structure, and composition of the sample. The secondary electron emission varies with the surface morphology of the sample, and the backscattered electron emission varies with the atomic number of elements in the sample. Therefore, the secondary electron probe (SE) can reflect the surface structure and morphology information of the sample, and the backscattered electron probe (BSE) can reflect the composition information of the sample. When the SEM is equipped with an energy-dispersion spectrometer or spectrometer, X-ray signals can be used to obtain qualitative or quantitative chemical composition analysis data of samples.

Trace element analysis of pyrite was conducted with a New Wave UP 213 Nd: YAG Laser Ablation (LA) system connected to a Thermo Element II ICP-MS at the MRL Key Laboratory of Metallogeny and Mineral Assessment, Institute of Mineral Resources, Chinese Academy of Geological Sciences (CAGS Beijing). Detailed operating conditions for the LA-ICP-MS instrument and data reduction were as described by [48,49]. Helium was used as a carrier gas, while argon was used as a makeup gas and mixed with the helium via a T-connector before entering the ICP. By adjusting the helium and argon flow, the optimal signal strength and stability of NIST SRM 612 were obtained to optimize the experimental conditions and control the oxidation yield to <0.3%. Each analysis was performed with 40 μm laser spot size and 10 Hz frequency and included a 20 s gas-blank background acquisition followed by 40 s sample data acquisition. Elemental contents of sulfides were calibrated against multiple reference materials (NIST SRM 610, MASS-1) using ^{57}Fe as the internal standard [49–53].

5. Results

5.1. Mass Balance Calculation

Al and Ti are generally considered immobile in hydrothermal alteration, yet Al can also be mobilized during high-temperature alteration/metamorphism [54,55]. In particular, a small amount of Al precipitates out during the sericitization process [56]. The sericitization of the Wulong deposit showed that Al is not suitable to be used as an immobile component to study the migration and enrichment of elements during hydrothermal alteration. So, TiO_2 is selected as the immobile component in this study. The migration and enrichment of elements during silicic alteration at Wulong can be expressed in the formula $\Delta C_i = C_i^A/k - C_i^o$, with C_i^o representing the content of the *i*th element in the unaltered rock. C_i^A denotes the content of the *i*th element in the altered rock. $K = M^o/M^A = C^A/C^o$, with C^o and C^A representing the mass of inactive elements in the unaltered and altered rock, respectively. M^o and M^A denote the mass of the unaltered and altered rock, respectively [16,54,55,57–59].

Mass balance calculation results show that during silicification, Al_2O_3 , CaO , Fe_2O_3 , K_2O , SiO_2 , Ag, As, Cu, and Pb were brought into the system, whereas MgO , Na_2O , FeO , Cr, Zn, and Ni were leached away (Table 1; Figure 6).

5.2. Geochemical Trends of Pyrite

Backscattered electron (BSE) images shows that Py1 occurs as euhedral grains, ranging in size from 50 to 500 μm , and has voids in the core (Figure 7). There is no zonal structure in Py1 (Figure 7).

The trace element compositions of Py1 were obtained by LAICP-MS analyses, including 25 spots on Py1. However, the previously reported data of the pyrite from [12] were also cited and discussed. All the analytical spots aim at pyrite without visible mineral inclusions, but the results suggest that some spots (Py1 and Py2, especially) encountered micro-inclusions even though they were not visible under microscope. These spots show irregular peaks such as Co, Ni, Cu, Zn, As, Ag, Sb, Au, Pb, and Bi. In some cases, Au and Ag peaks coincide, suggesting a gold mineral inclusion, and in other cases, Bi-Pb-Ag-Sb peaks overlap, suggesting a sulfosalt inclusion. Some grain boundaries show obvious overlapping signals of multiple elements, indicating that the laser may have encountered multiple minerals. The results of pyrite that are shown to be contaminated by inclusions have been excluded for subsequent studies, and the full results are listed in Table 2.

The gold content in the three stages of pyrite also varied greatly, ranging from 0.01~0.16 ppm. Py1 had the largest amount of invisible gold content in the deposit, ranging from 0.01 to 0.12 ppm. The gold content ranged from 0.02 to 0.07 ppm in Py2 and was slightly lower than Py1. The gold content of Py3 was similar with Py1 and Py2 and ranged from 0.02 to 0.16 ppm (Table 2). The gold content of three spots on Py3 were lower than their respective detection limits (Figure 8a). Silver contents of Py1 and Py3 were similar. Silver contents of Py2 were a little higher than those of Py1 and Py3 (Figure 8b). Lead contents were higher in Py3 and slightly lower in Py2 and Py1 (Figure 8c). Zinc contents were higher in Py1 but were significantly lower in Py2 and Py3 (Figure 8d). Copper and arsenic contents slightly increased from Py1 to Py3 (Figure 8e,f). Copper contents of Py1, Py2, and Py3 were 0.12~9.65 ppm, 0.06~10.00 ppm, and 0.35~13.20 ppm, respectively (Table 2). Arsenic contents of Py1, Py2, and Py3 were 0.36~495.00 ppm, 0.10~1219.00 ppm, and 0.20~1840.00 ppm, respectively (Table 2). The cobalt, nickel, and bismuth contents slightly decreased from Py1 to Py3 (Figure 8g–i). Stibium contents of Py1, Py2, and Py3 were 0.07~5.91 ppm, 0.01~4.60 ppm, and 0.40~6.79 ppm, respectively (Table 2).

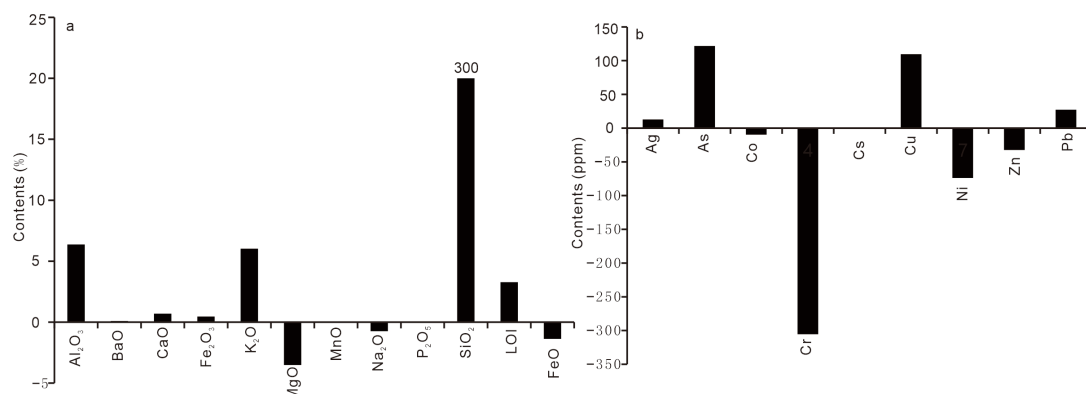


Figure 6. Gain–loss diagram for elements in Silicic alteration processes in the Wulong gold deposit (data listed in Table 1). (a) Gain–loss diagram for major elements in Silicic alteration processes; (b) Gain–loss diagram for trace elements in Silicic alteration processes.

Table 1. Major and trace elements of the least altered and silicified microdiorite samples from the Wulong gold deposit.

Sample	W81030-3	W81030-9	W81030-15	W81030-16	W81030-19	W81031-2	W81031-4	W81101-10	W81030-5	W81031-6	W81101-5	W81101-6
Rock	Fresh Rock	Fresh Rock	Fresh Rock	Fresh Rock	Fresh Rock	Fresh Rock	Fresh Rock	Fresh Rock	Silicified Rock	Silicified Rock	Silicified Rock	Silicified Rock
Al ₂ O ₃	16.06	16.81	11.67	12.15	15.85	15.76	10.70	16.35	5.87	0.06	13.78	0.31
BaO	0.08	0.09	0.02	0.05	0.06	0.05	<0.01	0.13	0.09	<0.01	0.06	<0.01
CaO	6.61	4.60	7.47	6.02	4.08	5.32	0.36	4.26	1.00	0.06	4.07	0.20
Fe ₂ O ₃	6.91	5.56	7.96	6.35	7.22	7.82	5.74	4.87	0.28	0.43	5.99	0.05
K ₂ O	2.04	3.00	3.44	4.61	2.14	3.20	2.38	4.95	4.06	<0.01	4.71	0.13
MgO	6.21	3.33	9.47	8.26	7.05	7.06	3.53	2.03	0.05	<0.01	2.20	0.02
MnO	0.11	0.05	0.14	0.12	0.06	0.08	0.03	0.07	0.02	<0.01	0.06	<0.01
Na ₂ O	3.35	3.29	0.09	1.28	2.76	2.58	0.15	1.89	0.49	0.01	0.63	0.01
P ₂ O ₅	0.16	0.21	0.07	0.27	0.14	0.16	0.10	0.18	0.01	<0.01	0.16	<0.01
SiO ₂	56.70	59.43	44.69	49.46	54.98	54.58	72.66	57.64	86.78	98.15	59.95	98.58
LOI	1.51	2.58	14.17	10.04	5.11	2.14	3.52	6.24	1.08	0.39	6.69	0.45
FeO	5.51	4.24	6.01	4.79	5.59	6.27	3.51	3.39	0.20	0.35	2.81	0.05
Ag	0.01	0.03	0.09	0.22	0.40	0.01	1.79	0.45	0.01	2.35	10.15	0.13
As	2.90	4.00	19.00	48.10	14.00	2.60	35.30	9.20	3.00	4.80	122.50	3.20
Co	24.70	14.70	33.10	32.70	30.60	22.80	8.00	10.10	0.20	0.80	10.90	0.10
Cr	297.00	27.00	642.00	541.00	492.00	399.00	214.00	23.00	<1.00	1.00	21.00	1.00
Cs	2.18	17.00	6.28	4.74	7.07	12.00	3.42	8.34	0.89	0.04	6.28	0.12
Cu	22.50	21.20	16.30	22.50	13.70	10.70	19.80	27.60	6.70	3.10	112.50	1.80
Ni	54.20	10.20	131.00	254.00	105.00	60.30	31.30	6.30	<0.2	1.50	5.90	<0.20
Pb	5.40	4.60	3.20	6.80	7.00	1.80	10.70	6.70	5.50	9.10	16.40	0.90
Zn	81.00	38.00	75.00	79.00	65.00	78.00	28.00	47.00	5.00	<2.00	21.00	2.00

Al₂O₃, BaO, CaO, Fe₂O₃, K₂O, MgO, MnO, Na₂O, P₂O₅, SiO₂, LOI, and FeO are in wt.%; The other elements are in ppm.

Table 2. LA-ICP-MS spot analysis data of Py1 to Py3.

Stage	Sample	Co	Ni	Cu	Zn	As	Ag	Sb	Au	Pb	Bi	References
1	30-5_1	168.07	65.42	0.26	1.59	0.40	951.39	104.78	0.12	177,698.20	85,829.09	This paper
	30-5_2	227.86	127.37	5.78	4.64	0.59	4.66	0.68	0.10	57.85	177.93	This paper
	30-7_2	0.01	<	28.04	51.69	0.76	0.05	0.37	0.10	1.17	0.15	This paper
	30-7_3	229.04	8.83	0.46	1.64	<	0.21	<	<	90.75	0.96	This paper
	30-7_4	233.77	28.88	<	1.36	<	1.32	<	0.02	112.85	7.90	This paper
	30-8_1	0.10	0.35	<	0.12	<	0.47	<	0.05	13.44	1.01	This paper

Table 2. Cont.

Stage	Sample	Co	Ni	Cu	Zn	As	Ag	Sb	Au	Pb	Bi	References
	30-10_1	1190.01	3760.94	1.09	3.20	0.36	<	<	0.02	0.19	0.83	This paper
	30-10_2	1227.76	4316.21	<	1.49	<	0.09	<	<	0.59	2.73	This paper
	30-10_3	1287.21	4625.49	0.36	<	0.00	<	0.17	<	0.48	2.17	This paper
	31-2_1	125.98	136.62	43.37	10.85	2.16	0.51	3.31	0.11	41.89	15.84	This paper
	31-2_2	353.62	910.16	2.95	6.50	12.09	0.09	1.39	0.01	8.70	3.59	This paper
	31-2_3	30.01	12.53	2.33	0.90	2.18	0.03	1.33	<	8.04	1.53	This paper
	31-2_4	28.79	113.82	9.65	5.92	8.83	0.35	2.07	0.06	41.32	11.10	This paper
	31-5_1	246.40	946.05	1.81	1.28	2.96	4.24	<	0.01	2.40	34.35	This paper
	31-5_2	0.54	1.66	6.55	4.74	29.53	1.92	5.91	0.02	22.35	0.07	This paper
	31-5_3	345.98	528.30	<	3.30	<	<	<	<	0.83	1.30	This paper
	31-6_1	80.46	2552.55	185.14	1083.31	<	19.35	<	<	197.17	32.36	This paper
	01-3_1	207.66	488.07	7.67	2.09	0.85	2.11	1.35	0.05	6.43	10.20	This paper
	01-3_2	205.57	283.48	2.03	3.87	<	1.47	0.21	0.02	1.43	3.17	This paper
	01-8_1	0.61	15.63	2.47	4.91	1.34	9.18	0.34	0.04	1008.80	1001.23	This paper
	01-8_2	0.18	<	<	0.25	<	0.01	0.32	<	0.36	0.07	This paper
	02-5_1	15.50	24.79	1.37	3.18	<	0.07	0.33	0.02	23.37	6.32	This paper
	02-7_1	0.03	3.71	1.34	3.16	6022.85	<	<	0.29	0.28	0.01	This paper
	02-7_2	9.09	1372.98	8.00	4.86	1078.58	1.89	3.99	1.28	292.09	12.02	This paper
	02-7_3	110.70	1487.17	100.60	2.60	787.30	1.18	0.07	0.06	83.01	14.92	This paper
	02-7_4	0.09	0.23	447.00	9.16	3170.68	2.78	1.60	1.89	143.90	7.36	This paper
	1-1-1	0.13	<	0.17	<	784.00	<	<	<	0.17	0.01	[12]
	1-1-2	45.10	6.69	0.46	<	868.00	4.92	0.25	0.02	68.70	2.08	[12]
	2-1-1	2.18	1.06	0.23	<	233.40	0.17	<	<	1.14	0.06	[12]
	2-1-2	0.09	<	0.99	<	240.90	<	<	<	0.20	0.01	[12]
	3-1-1	6.10	6.90	0.50	<	479.00	0.85	<	<	11.20	1.02	[12]
	3-1-2	61.40	11.70	1.57	<	164.60	1.76	<	<	22.30	2.54	[12]
	3-2-1	0.67	0.54	0.14	0.19	495.00	0.04	<	<	0.44	0.05	[12]
	3-2-2	4.93	1.11	0.12	<	20.30	3.23	<	<	26.80	1.40	[12]
	1-1-1	64.00	0.65	0.14	<	<	<	<	<	0.34	0.00	[12]
	1-1-2	28.70	9.08	23.10	0.16	<	0.48	<	<	28.70	0.02	[12]
	2-1-1	0.86	0.07	1.35	0.18	<	0.12	0.08	<	17.30	0.02	[12]
	2-1-2	109.10	21.60	1.33	0.24	<	0.35	<	<	16.70	0.06	[12]
	2-1-3	240.00	39.30	4.15	<	0.10	0.60	0.20	<	30.60	0.04	[12]
	2-1-4	11.80	2.41	19.60	8.40	0.20	0.70	0.63	0.03	78.50	0.15	[12]
	3-1-1	6.20	0.27	0.24	<	1219.00	0.18	0.07	0.07	10.90	0.35	[12]
	3-2-1	129.00	0.53	0.41	0.19	4040.00	0.04	0.09	2.22	4.60	0.15	[12]

Table 2. Cont.

Stage	Sample	Co	Ni	Cu	Zn	As	Ag	Sb	Au	Pb	Bi	References
	3-3-1	4.58	0.12	0.06	0.18	564.00	<	<	<	0.12	0.01	[12]
	1-1-1	1.14	6.48	0.24	<	121.00	2.10	0.07	<	7.40	0.50	[12]
	1-1-2	0.93	3.73	0.36	0.09	131.00	4.29	0.38	0.03	12.20	2.25	[12]
	1-2-1	92.60	23.20	10.00	<	60.00	11.40	15.90	0.03	89.40	16.90	[12]
	1-3-1	23.50	8.63	0.52	<	841.00	0.45	0.49	0.02	4.29	0.55	[12]
	1-4-1	0.34	<	0.22	0.10	55.40	0.05	0.01	<	0.38	0.04	[12]
	2-1-2	1.01	4.17	21.00	290.00	540.00	137.00	4.60	0.34	1550.00	32.70	[12]
	2-1-3	7.35	4.30	1.22	<	5890.00	650.00	0.10	2.69	2.66	0.28	[12]
	2-2-2	6.70	3.26	0.30	<	620.00	11.30	0.07	0.07	2.80	0.24	[12]
	2-2-3	23.40	42.00	2.08	0.13	253.00	10.20	2.14	0.02	41.00	4.20	[12]
	2-3-2	26.30	1.74	5.40	<	230.00	48.30	1.62	0.04	125.00	7.90	[12]
	2-3-3	568.00	31.40	0.23	<	0.90	0.52	0.06	<	2.68	0.13	[12]
	2-4-2	84.40	0.81	0.15	0.13	2.50	0.18	0.06	<	1.10	0.08	[12]
	2-5-3	65.60	1.53	0.18	<	6.30	0.92	0.23	<	5.20	0.32	[12]
	2-5-4	68.40	8.05	0.12	<	19.80	4.20	0.19	<	19.60	0.76	[12]
	2-6-2	20.40	1.36	50.00	0.26	600.00	42.40	1.76	0.03	147.00	7.30	[12]
	2-8-2	1.48	1.59	123.00	0.55	0.20	8.90	0.40	<	21.50	1.66	[12]
3	1-1-1	14.49	0.37	13.20	0.34	10.60	2.58	2.39	<	46.20	0.00	[12]
	1-1-2	0.63	0.07	0.35	0.14	118.50	0.06	0.41	<	8.50	0.00	[12]
	2-1-1	2.77	1.75	10.70	0.84	1840.00	2.77	15.50	0.16	217.00	0.04	[12]
	2-1-2	0.80	<	1.94	0.17	77.00	0.80	6.79	0.02	34.50	<	[12]

All units are in parts per million (ppm); < = below the detection limit.

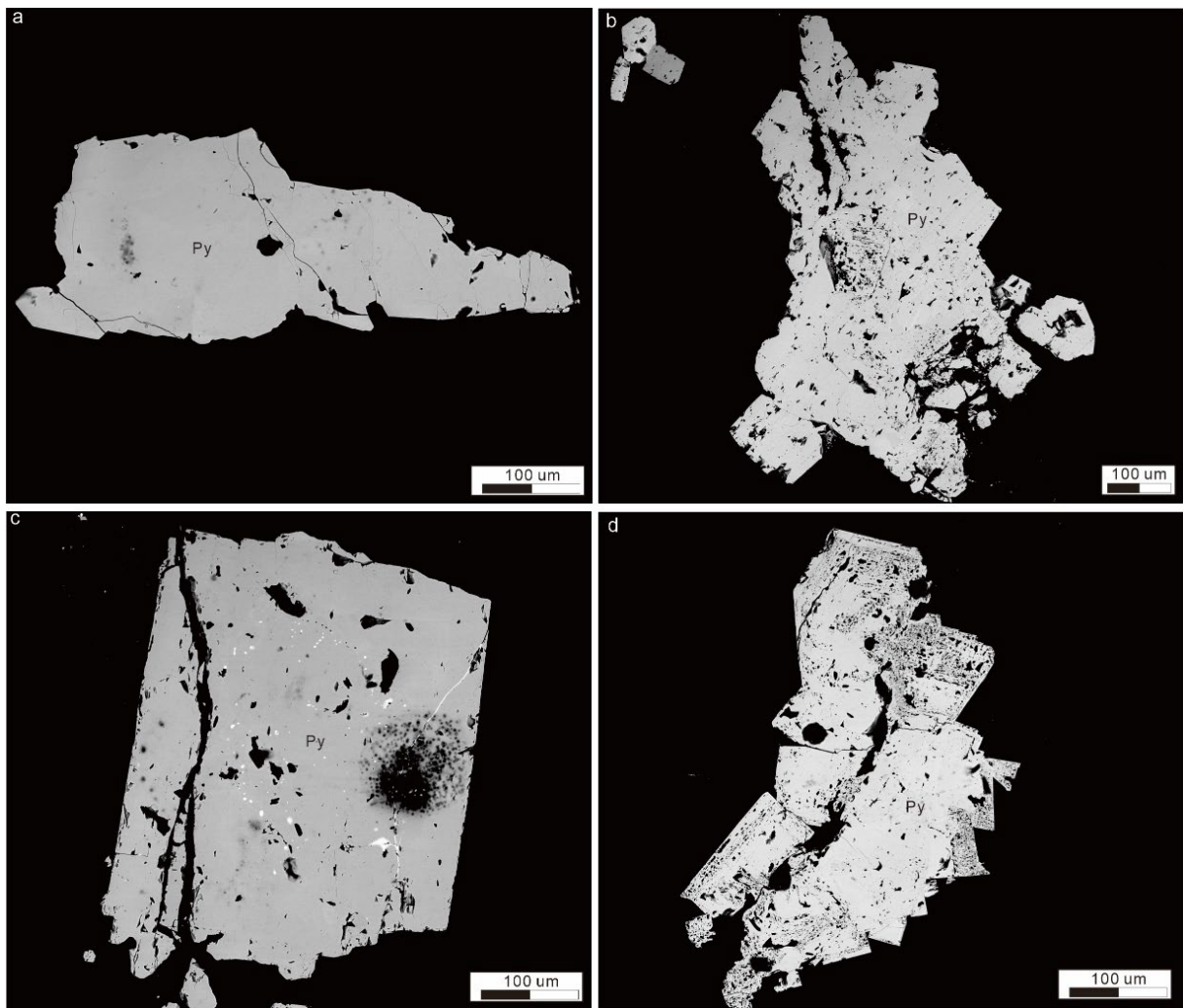


Figure 7. (a–d) Backscattered electron images showing the textural characteristics of Py1.

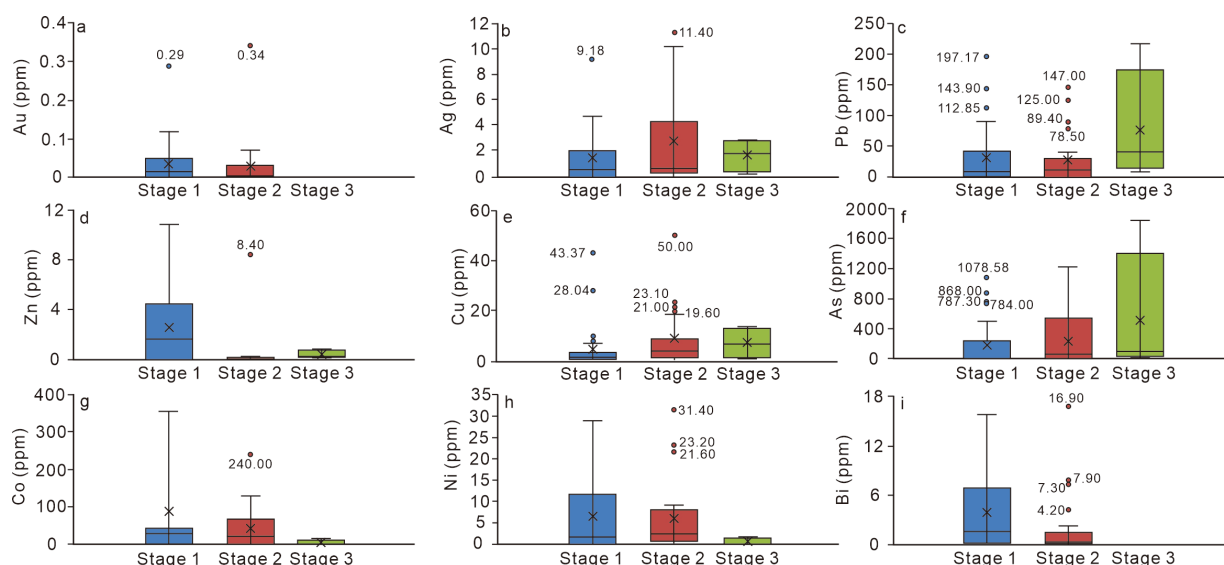


Figure 8. Box plot of LA-ICP-MS trace elemental contents of Py1 to Py3 (data listed in Table 2). (a) Box plot of Au contents of Py1 to Py3; (b) Box plot of Ag contents of Py1 to Py3; (c) Box plot of Pb contents of Py1 to Py3; (d) Box plot of Zn contents of Py1 to Py3; (e) Box plot of Cu contents of Py1 to Py3; (f) Box plot of As contents of Py1 to Py3; (g) Box plot of Co contents of Py1 to Py3; (h) Box plot of Ni contents of Py1 to Py3; (i) Box plot of Bi contents of Py1 to Py3.

6. Discussion

6.1. Migration and Enrichment of Elements

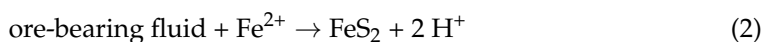
A substantial amount of SiO_2 was likely brought into the hydrothermal system during silicic alteration, and the strength of silicification near the mineralized zone was stronger than that in the area away from the mineralized zone. This is related to the increase of the strength of silicification throughout the hydrothermal alteration process. This also shows that silicification is ore-related at Wulong. K_2O was brought into the system, whereas Na_2O was leached away. K_2O and Na_2O repel each other and are incompatible. As the K^+ and Na^+ components either increased, the other decreased [60]. CaO was brought into the system, which is related to the emergence of carbonate. Fe_2O_3 was brought into the system, which shows that the precipitation of pyrite and the hematite occurs on the surface of feldspar and altered minerals in the form of microparticles. FeO was leached away, which shows that the mineralization alteration process is accompanied by the change of oxygen fugacity of the system, and Fe_2O_3 is more likely to be converted from FeO in the alteration system [60–62]. At the same time, iron-rich minerals such as pyrite and chalcopyrite are commonly found in the Wulong deposit. This indicates that the migration of Fe^{2+} and Fe^{3+} may be affected by various occurring forms during hydrothermal alteration [63]. There are generally two types of As-bearing pyrite. The first type is $\text{Fe}(\text{S}, \text{As})_2$, which is formed by As^{1-} instead of S [64,65]. The second type is $(\text{Fe}, \text{As})\text{S}_2$, which is formed by As^{3+} instead of Fe [66]. It is generally believed that the substitution of As into the pyrite lattice structure would increase the gold carrying capacity in the gold-bisulfide complex [67,68]. During silicification at Wulong, a large number of As elements migrated in and FeO migrated out. This suggests that chemical formula of pyrite is $(\text{Fe}, \text{As})\text{S}_2$, which is formed by As^{3+} instead of Fe at Wulong [66]. The precipitation of chalcopyrite and galena during silicic alteration resulted that Cu and Pb were brought into the hydrothermal system. During silicification, Ag also was brought into the system because of the positive correlation between Au and Ag in gold deposits [69–71].

The symbiosis of silicification, sericite, and pyrite can be seen in the study area, indicating that acidic ore-bearing fluids with high sulfur content are generally developed [10]. During silicification, K_2O was brought into the system, whereas Na_2O was leached away,

and sericite alteration occurred at the same time. The fact that K_2O was brought into the system and Na_2O was leached away indicates that the silicification is caused by plagioclase alteration rather than potassium feldspar alteration [10]. The process of silicification followed the reaction (1):



During the process of silicification, ore-bearing fluid migrates upward. Temperature and pressure gradually decrease, and oxygen fugacity increases during the process [10]. When the oxygen fugacity increases, the ore-bearing fluid is weakly acidic, and the conditions of weak acidity, the decrease of temperature and pressure, and the increase of oxygen fugacity promote the precipitation of SiO_2 , resulting in the silicification [10,12,57]. In the process of silicification, the content of H^+ reduces, and the pH value of the fluid increases. The ore-bearing fluid is weakly alkaline, which can promote the precipitation of pyrite. The process followed the reaction (2):



During the precipitation of pyrite, the content of HS^- is reduced in the ore-bearing fluid [10,12,57]. Au is mainly transported in the form of $Au(HS)^{2-}$ at the Wulong deposit, which is discussed in detail below. The depleted HS^- concentration in the ore-forming fluids enhanced the precipitation of Au, resulting in gold precipitation.

6.2. Trace Element Distribution and Pyrite Genesis

Py1 is relatively rich in Au and Zn contents and lacking in Pb, Cu, and As contents. Py2 is relatively rich in Au and Cu contents and lacking in Pb and Zn contents. Py3 is relatively rich in Pb, Cu, and As contents and lacking in Au, Zn, Co, Ni, and Bi contents. The Ag contents are similar in the different generations of pyrite. There is no correlation between Au vs. As, Au vs. Cu, Au vs. Ag, or Au vs. Sb contents in the different generations of pyrite. Positive correlations are found in Pb vs. Sb, Sb vs. Ag, Ag vs. Pb, Pb vs. Bi, and Co vs. Ni (Figure 9).

The change in trace element composition of the later hydrothermal pyrites, compared to the diagenetic pyrites, is probably due to a number of factors, including the ability of the trace elements to substitute for Fe^{2+} and S^{2-} in the pyrite structure and the metal availability and solubility in the hydrothermal fluid [72–74]. Pb, Zn, Cu, Ag, Ni, and Mo are commonly present at much lower levels in metamorphic and hydrothermal pyrite compared to early diagenetic pyrite. This suggests that the recrystallization of diagenetic pyrite to produce euhedral metamorphic pyrite is accompanied by a release of certain trace elements in the pyrite structure [35,75–79]. At the Wulong deposit, invisible gold was released by this process to form native gold and gold telluride inclusions in later pyrite generations [75]. Our data suggest that the trace elements (Ni, Co, As, and Se) which have the ability to form limited solid-solution series with pyrite are not released during pyrite recrystallization and tend to concentrate in most euhedral metamorphic and hydrothermal pyrites, forming discrete growth zones in the pyrite, possibly related to metal diffusion or fluid flow during recrystallization [76–80]. This is not the case for most other trace elements (e.g., Pb, Cu, Zn, Ag, Te, and Au), due possibly to their larger ionic size and/or different charge, which leads them to form discrete mineral inclusions (galena, chalcopyrite, sphalerite, tellurides, and free gold) within the later metamorphic and/or hydrothermal pyrite [76,81].

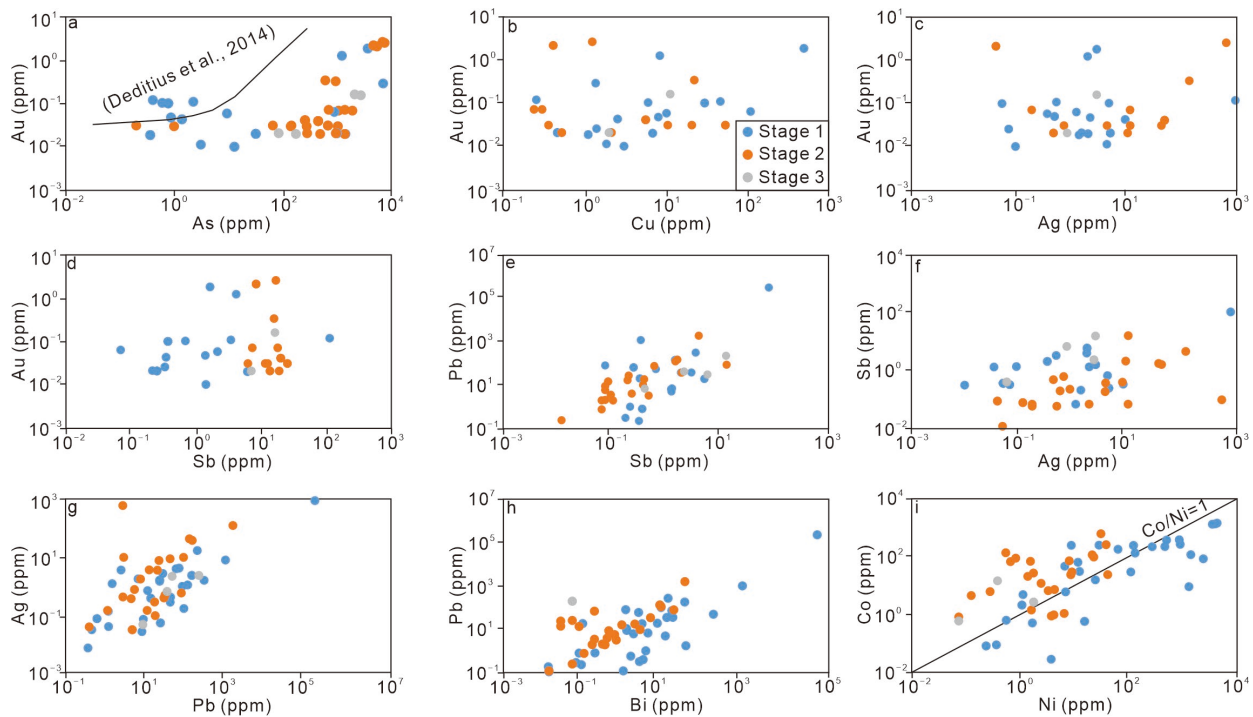


Figure 9. Binary plots of (a) Au vs. As, (b) Au vs. Cu, (c) Au vs. Ag, (d) Au vs. Sb, (e) Pb vs. Sb, (f) Sb vs. Ag, (g) Ag vs. Pb, (h) Pb vs. Bi, and (i) Co vs. Ni of Py1 to Py3.

In the Wulong gold deposit, the migration and enrichment of ore-forming elements in the fluid can be reflected by the pyrite structure and geochemical characteristics of some trace elements. The differences in the distribution of “invisible” chalcophile minerals in pyrite reflect the changes in the ability of elements to differentiate in fluids. Arsenic is also one of the important trace elements in pyrite, and its content is considered to be an important indicator of gold enrichment. Simon et al. (1999) have already proved that the occurrence state of arsenic is As^- in gold-bearing arsenic pyrite by X-ray absorption near-edge structure analyses [64]. The previous research also suggested that gold is present as sub-micrometer size inclusion (Au^0) and lattice gold in arsenic pyrite (Au^+). Cook and Chrystoullis (1990) found that the concentrations of arsenic and gold in pyrite are positively correlated [82]. This shows that the development of arsenic in pyrite is more conducive to the enrichment of gold, and gold and arsenic exist stably by replacing iron and sulfur in the crystal lattice of pyrite, respectively [81].

According to the microscopic observations, a large amount of native gold and electrum are developed in the Wulong gold deposit (Figure 4a,b), which was also reported in a previous study [83]. The presence of invisible gold is also indicated by the mineral chemistry of pyrite presented in this study. The micron-size native gold occurs in granular form in quartz fissures of Py2 (Figure 4a,b). Native gold may have been precipitated directly from hydrothermal fluid. The high invisible Au content and micron-size native gold in Py2 reveal that the hydrothermal fluid of the middle stage may have been saturated with respect to Au.

Bismuth contents of Py1 and Py2 were higher than that in Py3 of the Wulong deposit. This is consistent with the result of microscopic observation that the bismuthinite only developed in the stage 1 and stage 2 of mineralization. Bismuthinite is often associated with gold. Native gold is often found in or around bismuthinite. The molten states of native bismuth can absorb gold in the fluid and form the combination of natural gold and natural bismuth [84]. Bismuth element plays an important role in gold precipitation of the Wulong gold deposit.

The highest lattice-gold content in pyrite (i.e., solid solution) can be expressed in $C_{Au} = 0.02 \times C_{As} + 4 \times 10^{-5}$. The Au/As ratios above the “gold solubility line” indicate that gold likely occurs as nanoparticles, and those below the line indicate that gold likely occurs as a solid solution (Au^+) [76,85,86]. The Au–As diagram shows that most pyrite data points fall below the Au solubility line (Figure 9a), indicating that most of invisible gold occurs as solid solution (Au^+) [72,86].

The Co/Ni ratio is commonly used to indicate the pyrite genesis in gold deposits [87,88]. Volcanogenic pyrite commonly has Co/Ni ratio above 1 (up to 10) [88,89]. Diagenetic pyrite commonly has Co/Ni ratio below 1 (often around 0.63) [89]. Hydrothermal pyrite commonly has a highly variable Co/Ni ratio (mostly above +1) [87,88], which is observed in all Py1 to Py3 from the Wulong gold deposit.

6.3. Ore-Forming Process

Fluid inclusions studies of stage 1 quartz indicated that inclusions were of medium-high homogenization temperatures (283–395 °C), and varying salinities (0.70–8.95 wt.% NaCl_{eqv}), trapping pressures (184–380 MPa), and CO₂ densities (0.24–0.81 g/cm³), and belonged to a H₂O–CO₂–NaCl fluid system. The ore-forming fluids of stage 2 were of medium temperatures (219–328 °C) and varying salinities (0.18–7.86 wt.% NaCl_{eqv}), pressures (135–307 MPa), and CO₂ densities (0.18–0.79 g/cm³), and belonged to a H₂O–CO₂–NaCl ± CH₄ ± N₂ fluid system. Stage 3 fluids were of low temperatures (144–255 °C) and varying salinities (0.18–4.96 wt.% NaCl_{eqv}) and belonged to a H₂O–NaCl fluid system [12,90]. Stage 3 fluids also contain CO₂, H₂S, and CH₄. Fluid immiscibility of the H₂O–CO₂ fluids was recorded by the coexistence of different fluid inclusion assemblages [12].

When the ore-forming fluid is at 250–350 °C, Au is mainly transported in the form of $Au(HS)^{2-}$. If the ore-fluid is H₂S poor (<10^{−4} mol/L), Cl[−]-rich (>0.5 mol/L), and low pH (<4.5), Au is mainly transported in the form of $AuCl_2^-$ [91]. The Wulong ore-fluid was low-medium temperatures (144–395 °C) and low-medium salinities (0.18–8.95 wt.% NaCl_{eqv}). Moreover, the presence of sericite represents weakly acidic fluid conditions [25]. This suggests that Au was mainly transported in the form of $Au(HS)^{2-}$ at Wulong.

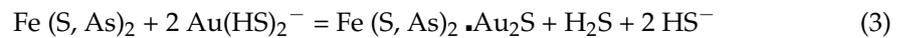
Gold precipitation can occur in the following four ways: (1) Hydrothermal fluid–wallrock reactions increase the fluid oxygen fugacity; (2) Fluid boiling that leads to fluid H₂S degassing, which destabilizes the $Au(HS)^{2-}$ complexes; (3) Meteoric water incursion that dilutes the fluid sulfur content; (4) Sulfur leached from pre-existing sulfides into the ore fluids, which promotes chemisorption and thus gold precipitation [92–96]. At Wulong, the ascending ore-forming fluids may have reacted with the microdiorite, causing silicification and pyritization. There were elemental migration/enrichment and fluid immiscibility during the alteration. Temperature and pressure of the ore-forming fluids dropped from stage 1 to stage 3, which would result in fluid immiscibility and degassing (CO₂ and H₂S) [12]. The decrease of reducing volatiles in the fluid would have increased the oxygen fugacity [92,97], further promoting gold precipitation at Wulong.

Silicification and pyritization are ore-related and widely developed at Wulong. The water–rock reaction of silicification would have changed the fluid physicochemical conditions (the depleted H⁺ concentration and HS[−] concentration in the ore-forming fluids), and led to the precipitation of pyrite, gold, bismuthinite, galena, sphalerite, and chalcopyrite.

Bismuth migrates mainly in the form of bismuth complex ($Bi_2S_2(OH)_2^0$, $HBi_2S_4^-$) in sulfur-rich fluids, but it migrates mainly in the form of bismuth complex ($BiCl_2^-$) in chlorine-rich fluids [84]. The characteristics of the fluid and the composition of metal sulfide indicate that the ore-forming fluid is rich in sulfur. So, bismuth migrates mainly in the form of bismuth complex ($Bi_2S_2(OH)_2^0$, $HBi_2S_4^-$) at Wulong. When the temperature decreases and sulfur is depleted in the hydrothermal fluid, desulfurization occurs and the bismuth complex releases natural bismuth. The molten states of native bismuth can absorb gold in the fluid and form the combination of natural gold and natural bismuth [84].

At stage 1, pyrite is rich in Au and Zn contents and lacking in Pb, Cu, and As contents. The ore-forming fluid was likely CO₂-rich (belonging to the H₂O–CO₂–NaCl system) and

reacted with the microdiorite to form silicification. At this stage, Au was likely transported as sulfide complexes (such as $\text{Au}(\text{HS})_2^{2-}$ complex in a neutral pH region) [97–102]. The precipitation of Au followed the reaction (3) and/or reaction (4).



These two reactions show that the H_2S activity has a strong influence on the precipitation of Au, regardless of Au occurring as either a solid solution (Au^+), or native gold (Au^0). The widely distributed pyrite in all stages of the Wulong deposit is closely related to Au precipitation and likely depleted the H_2S concentration in the ore-forming fluids, which enhanced the precipitation of Au [81,103]. Therefore, the depleted H^+ concentration and HS^- concentration in the ore-forming fluids lead to instability of the $\text{Au}(\text{HS})_2^{2-}$ complexes during the process of silicification and pyritization [98]. Moreover, the depleted sulfur and the reduced temperature during silicification and pyritization lead to the precipitation of gold and bismuthinite. The inclusions of stage 1 are of medium-high homogenization temperatures (283–395 °C). The temperatures are a little higher for the precipitation of gold and bismuthinite [84]. Only a small amount of bismuthinite can be found at stage 1. The gold may have then precipitated in the form of a solid solution in pyrite, accompanied by the precipitation of pyrite, bismuthinite, galena, and sphalerite (Figure 10a).

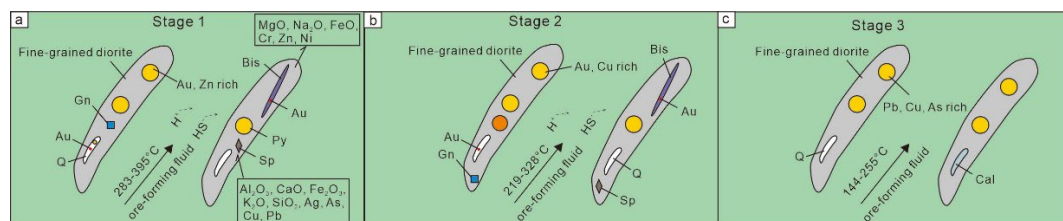


Figure 10. Schematic diagram of stage 1 to 3 gold deposition mechanism of the Wulong gold deposit. (a) Schematic diagram of stage 1 gold deposition mechanism; (b) Schematic diagram of stage 2 gold deposition mechanism; (c) Schematic diagram of stage 3 gold deposition mechanism.

At stage 2, pyrite is rich in Au-Cu contents but lacking in Pb-Zn contents. The ore-forming fluid belonged to the $\text{H}_2\text{O}-\text{CO}_2-\text{NaCl} \pm \text{CH}_4 \pm \text{N}_2$ system and had lower temperatures, salinities, pressures, and CO_2 densities than those of stage 1. The depleted H^+ concentration and HS^- concentration in the ore-forming fluids lead to instability of the $\text{Au}(\text{HS})_2^{2-}$ complexes during the process of silicification and pyritization [97–100]. The depleted sulfur and the reduced temperature during silicification and pyritization also lead to the precipitation of gold and bismuthinite. The metallic minerals precipitated are similar to those of Stage 1, but with chalcopyrite and more bismuthinite (Figure 10b).

At stage 3, pyrite is rich in Pb, Cu, and As contents and lacking in Au, Zn, Co, Ni, and Bi contents. The ore-forming fluid belonged to the $\text{H}_2\text{O}-\text{NaCl}$ fluids system and had lower temperatures and salinities than those of both stage 1 and 2. There were also CO_2 , H_2S , and CH_4 degassed from the stage 3 fluid [103], which further broke down the $\text{Au}(\text{HS})_2^{2-}$ complexes and precipitated the refractory gold in pyrite. Lower-temperature hydrothermal minerals, such as pyrite, quartz, calcite, sericite, and chlorite, were also precipitated (Figure 10c).

7. Conclusions

- (1) Alteration is well-developed in the mining area, including silicification, pyritization, sericitization, chloritization, and carbonatization, among which the former two are closely related to mineralization. Mass balance calculation results indicate that during silicification, certain elements (Al, Ca, Fe, K, Si, Ag, As, Cu, and Pb) entered the fluid system, whereas some others (Mg, Na, Fe, Cr, Zn, and Ni) were leached away. During the process of silicification, the content of H⁺ and HS[−] reduced in the ore-forming fluids.
- (2) LA-ICP-MS pyrite trace element analyses indicate that Py1 is relatively rich in Au and Zn contents and lacking in Pb, Cu, and As contents. Py2 is relatively rich in Au and Cu contents and lacking in Pb and Zn contents. Py3 is relatively rich of Pb, Cu, and As contents and lacking in Au, Zn, Co, Ni, and Bi contents.
- (3) The depleted H⁺ concentration and HS[−] concentration in the ore-forming fluids lead to instability of the Au(HS)₂[−] complexes during the process of silicification and pyritization. Moreover, the depleted sulfur and the reduced temperature during silicification and pyritization also lead to the precipitation of gold and bismuthinite.

Author Contributions: Conceptualization and writing, Z.Z.; review and editing, Y.W. and C.L.; formal analysis, J.H., D.L., H.Q. and F.L. All authors have read and agreed to the published version of the manuscript.

Funding: This research was funded by National Key R&D Program of China, grant number No. 2018YFC0603804 and Mine prospecting and prediction Special Project of Zijin Mining, grant number KCDZKCY-2022-048.

Data Availability Statement: All data generated or analysed during this study are included in this published article.

Acknowledgments: We thank the staffs from ALS Minerals (Guangzhou) for helping with the XRF analysis, and Chinese Academy of Geological Sciences (Beijing) for helping with the LA-ICP-MS analysis and backscattered electron (BSE) images. Our thanks also go to 103 Branch of Non-ferrous Geological of Liaoning Province Co., Ltd., for the field assistance.

Conflicts of Interest: I warrant the manuscript represents original work that is not being considered for publication, in whole or in part, in another journal, book, conference proceedings, or government publication with a substantial circulation. I warrant there are no conflict of interest.

References

1. Deng, J.; Wang, Q.F. Gold mineralization in China: Metallogenic provinces, deposit types and tectonic framework. *Gondwana Res.* **2016**, *36*, 219–274. [[CrossRef](#)]
2. Wang, Y.W.; Xie, H.J.; Li, D.D.; Shi, Y.; Liu, F.X.; Sun, G.Q.; Sun, Q.M.; Zhou, G.C. Prospecting prediction of ore concentration area exemplified by Qingchengzi Pb-Zn-Au-Ag ore concentration area, Eastern Liaoning Province. *Miner. Depos.* **2017**, *36*, 1–24. (In Chinese with English Abstract)
3. Feng, Y.C.; Qiu, K.F.; Wang, D.Z.; Sha, W.J.; Li, S. Forming conditions of tellurides and their constraints on gold enrichment in Linglong gold district, Jiaodong gold province. *Acta Petrol. Sin.* **2022**, *38*, 63–77. (In Chinese with English Abstract)
4. Yu, H.C.; Qiu, K.F.; Chew, D.; Yu, C.; Ding, Z.J.; Zhou, T.; Li, S.; Sun, K.F. Buried Triassic rocks and vertical distribution of ores in the giant Jiaodong gold province (China) revealed by apatite xenocrysts in hydrothermal quartz veins. *Ore Geol. Rev.* **2022**, *140*, 104612. [[CrossRef](#)]
5. Deng, J.; Yang, L.Q.; Groves, D.I.; Zhang, L.; Qiu, K.F.; Wang, Q.F. An integrated mineral system model for the gold deposits of the giant Jiaodong province, eastern China. *Earth-Sci. Rev.* **2020**, *208*, 103274. [[CrossRef](#)]
6. Wei, Y.J.; Qiu, K.F.; Guo, L.N.; Liu, X.D.; Tang, L.; Shi, Q.F.; Gao, X.K. Characteristics and evolution of ore-fluids of the Dayingezhuang gold deposit, Jiaodong gold province. *Acta Petrol. Sin.* **2020**, *36*, 1821–1832. (In Chinese with English Abstract)
7. Sai, S.X.; Qiu, K.F. Ore-forming processes of the Rushan gold deposit, Jiaodong: Fluid immiscibility under episodic fluid pressure fluctuations. *Acta Petrol. Sin.* **2020**, *36*, 1547–1566. (In Chinese with English Abstract)
8. Deng, J.; Qiu, K.F.; Wang, Q.F.; Goldfarb, R.J.; Yang, L.Q.; Zi, J.W.; Geng, J.Z.; Ma, Y. In-situ dating of hydrothermal monazite and implications on the geodynamic controls of ore formation in the Jiaodong gold province, Eastern China. *Econ. Geol.* **2020**, *115*, 671–685. [[CrossRef](#)]
9. Zeng, Q.D.; Chen, R.Y.; Yang, J.H.; Sun, G.T.; Yu, B.; Wang, Y.B.; Chen, P.W. The metallogenic characteristics and exploring ore potential of the gold deposits in eastern Liaoning Province. *Acta Petrol. Sin.* **2019**, *35*, 1939–1963. (In Chinese with English Abstract)

10. Wang, D.L. Genetic Mineralogy and Deep Prospects of Wu Long Gold Deposit in Liaoning Province. Master's Thesis, China University of Geosciences, Beijing, China, 2017. (In Chinese with English Abstract)
11. Liu, G.C.; Qian, X.; Li, J.; Zi, J.W.; Zhao, T.Y.; Feng, Q.L.; Chen, G.Y.; Hu, S.B. Geochronological and geochemical constraints on the petrogenesis of early Paleoproterozoic (2.40–2.32 Ga) Nb-enriched mafic rocks in southwestern Yangtze block and its tectonic implications. *J. Earth Sci.* **2020**, *31*, 35–52. [[CrossRef](#)]
12. Yu, B.; Zeng, Q.; Frimmel, H.E.; Wang, Y.B.; Guo, W.K.; Sun, G.T.; Zhou, T.C.; Li, G.P. Genesis of the Wulong gold deposit, northeastern North China Craton: Constraints from fluid inclusions, H-O-S-Pb isotopes, and pyrite trace element concentrations. *Ore Geol. Rev.* **2018**, *102*, 313–337. [[CrossRef](#)]
13. Gu, Y.C. The Mesozoic Tectonic-Magmatic Constraints on the Gold Mineralization in Wulong Gold Mining Area, Eastern Liaoning. Ph.D. Thesis, China University of Geosciences, Beijing, China, 2019. (In Chinese with English Abstract)
14. Wei, J.H.; Liu, C.Q.; Li, Z.D.; Zhao, Y.X. Simulation of rock mass balance of two typical altered rocks in Wulong gold deposit of Liaoning, China. *J. Cent. South Univ. Technol.* **2001**, *8*, 197–202. [[CrossRef](#)]
15. Tang, L.; Hu, X.K.; Santosh, M.; Zhang, S.T.; Spencer, C.J.; Jeon, H.; Zhao, Y.; Cao, H.W. Multistage processes linked to tectonic transition in the genesis of orogenic gold deposit: A case study from the Shangong lode deposit, East Qinling, China. *Ore Geol. Rev.* **2019**, *111*, 102998. [[CrossRef](#)]
16. Zhang, Z.C.; Li, N.; Ji, X.Z.; Han, Z.; Guo, Y.Y.; Li, Z.C. Hydrothermal alteration of the Anba deposit, Yangshan gold belt, western Qinling. *Acta Petrol. Sin.* **2015**, *31*, 3405–3419. (In Chinese with English Abstract)
17. Parsapoor, A.; Khalili, M.; Mackizadeh, M.A. The behavior of trace and rare earth elements (REE) during hydrothermal alteration in the Rangan area (Central Iran). *J. Asian Earth Sci.* **2009**, *34*, 123–134. [[CrossRef](#)]
18. Helba, H.A.; Khalil, K.I.; Abou, N.M.F. Alteration patterns related to hydrothermal gold mineralization meta-andesites at Dungash Area, Eastern Desert, Egypt. *Resour. Geol.* **2001**, *51*, 19–30. [[CrossRef](#)]
19. Yu, H.C.; Qiu, K.F.; Pirajno, F.; Zhang, P.C.; Dong, W.Q. Revisiting Phanerozoic evolution of the Qinling Orogen (East Tethys) with perspectives of detrital zircon. *Gondwana Res.* **2022**, *103*, 426–444. [[CrossRef](#)]
20. Yu, H.C.; Qiu, K.F.; Deng, J.; Zhu RMathieu, L.; Sai, S.X.; Sha, W.J. Exhuming and preserving epizonal orogenic Au-Sb deposits in rapidly uplifting orogenic settings. *Tectonics* **2022**, *41*, e2021TC007165. [[CrossRef](#)]
21. Long, Z.Y.; Qiu, K.F.; Santosh, M.; Yu, H.C.; Jiang, X.Y.; Zou, L.Q.; Tang, D.W. Fingerprinting the metal source and cycling of the world's largest antimony deposit in Xikuangshan, China. *GSA Bull.* **2022**. [[CrossRef](#)]
22. Hu, X.; Tang, L.; Zhang, S.T.; Tsunogae, T.; Santosh, M.; Sun, L.; Spencer, C.; Jeon, H.; Wang, L. Formation of the Qiyugou porphyry gold system in East Qinling, China: Insights from timing and source characteristics of Late Mesozoic magmatism. *J. Geol. Soc.* **2022**, *179*. [[CrossRef](#)]
23. Tang, L.; Wagner, T.; Fusswinkel, T.; Zhang, S.; Hu, X.; Schlegel, T. Fluid inclusion evidence for the magmatic-hydrothermal evolution of closely linked porphyry Au, porphyry Mo, and barren systems, East Qinling, China. *GSA Bull.* **2022**, *134*, 1529–1548. [[CrossRef](#)]
24. Tang, L.; Zhao, Y.; Zhang, S.T.; Sun, L.; Hu, X.K.; Sheng, Y.M.; Zeng, T. Origin and evolution of a porphyry-breccia system: Evidence from zircon U-Pb, molybdenite Re-Os geochronology, in situ sulfur isotope and trace elements of the Qiyugou deposit, China. *Gondwana Res.* **2021**, *89*, 88–104. [[CrossRef](#)]
25. Wei, Q.; Fan, H.R.; Lan, T.G.; Liu, X. Hydrothermal Alteration and Element Migration in the Sizhuang Gold Deposit, Jiaodong Province, China. *Bull. Mineral. Petrol. Geochem.* **2018**, *37*, 283–293. (In Chinese with English Abstract)
26. Jamtveit, B. Metamorphism: From Patterns to Processes. *Elements* **2014**, *6*, 149–152. [[CrossRef](#)]
27. Dugdale, A.L.; Wilson, C.J.L.; Squire, R.J. Hydrothermal alteration at the Magdala gold deposit, Stawell, western Victoria. *Aust. J. Earth Sci.* **2006**, *53*, 733–757. [[CrossRef](#)]
28. Chinnasamy, S.S.; Mishra, B. Greenstone metamorphism, hydrothermal alteration, and gold mineralization in the genetic context of the granodiorite-hosted gold deposit at Jonnagiri, Eastern Dharwar Craton, India. *Econ. Geol.* **2013**, *108*, 1015–1038. [[CrossRef](#)]
29. Craw, D. Geochemistry of late metamorphic hydrothermal alteration and graphitization of host rock, Macraes gold mine, Otago Schist, New Zealand. *Chem. Geol.* **2002**, *191*, 257–275. [[CrossRef](#)]
30. Wu, M.Q.; Samson, I.M.; Qiu, K.F.; Zhang, D.H. Concentration mechanisms of REE-Nb-Zr-Be mineralization in the Baerzhe deposit, NE China: Insights from textural and chemical features of amphibole and rare-metal minerals. *Econ. Geol.* **2021**, *116*, 651–679. [[CrossRef](#)]
31. Yang, J.H.; Wu, F.Y.; Wilde, S.A. A review of the geodynamic setting of large-scale late Mesozoic gold mineralization in the North China Craton: An association with lithospheric thinning. *Ore Geol. Rev.* **2003**, *23*, 125–152. [[CrossRef](#)]
32. Zhang, Z.C.; Wang, Y.W.; Li, D.D.; Lai, C. Lithospheric Architecture and Metallogenesis in Liaodong Peninsula, North China Craton: Insights from Zircon Hf-Nd Isotope Mapping. *Minerals* **2019**, *9*, 179. [[CrossRef](#)]
33. Yang, J.H.; Sun, J.F.; Zhang, J.H.; Wilde, S.A. Petrogenesis of Late Triassic intrusive rocks in the Northern Liaodong Peninsula related to decratonization of the North China Craton: Zircon U-Pb age and Hf-O isotope evidence. *Lithos* **2012**, *153*, 108–128. [[CrossRef](#)]
34. Suo, A.; Zhao, D.Z.; Zhang, F.S.; Wang, H.R.; Liu, F.Q. Driving forces and management strategies for estuaries in Northern China. *Front. Earth Sci. China* **2010**, *4*, 51–58. [[CrossRef](#)]
35. Yang, J.H.; Wu, F.Y.; Chung, S.L.; Wilde, S.A.; Chu, M.F. A hybrid origin for the Qianshan A-type granite, Northeast China: Geochemical and Sr-Nd-Hf isotopic evidence. *Lithos* **2006**, *89*, 89–106. [[CrossRef](#)]

36. Wu, F.Y.; Yang, J.H.; Wilde, S.A.; Zhang, X.O. Geochronology, petrogenesis and tectonic implications of Jurassic granites in the Liaodong Peninsula, NE China. *Chem. Geol.* **2005**, *221*, 127–156. [[CrossRef](#)]
37. Jing, Y.; Jiang, S.; Zhao, K.; Ni, P.; Ling, H.; Liu, D. Shrimp U-Pb zircon dating for lamprophyre from Liaodong Peninsula: Constraints on the initial time of Mesozoic lithosphere thinning beneath Eastern China. *Chin. Sci. Bull.* **2005**, *50*, 2612–2620. [[CrossRef](#)]
38. Wei, J.H.; Liu, C.Q.; Tang, H.F. Rb-Sr and U-Pb isotopic systematics of pyrite and granite in Liaodong gold province, North, China: Implication for the age and genesis of a gold deposit. *Geochem. J.* **2003**, *37*, 567–577. [[CrossRef](#)]
39. Duan, X.; Zeng, Q.; Yang, J.; Liu, J.; Wang, Y.; Zhou, L. Geochronology, geochemistry and Hf isotope of Late Triassic magmatic rocks of Qingchengzi district in Liaodong Peninsula, Northeast China. *J. Asian Earth Sci.* **2014**, *91*, 107–124. [[CrossRef](#)]
40. Zhang, G.R.; Jiang, S.E.; Han, X.P.; Huan, Z.F.; Qu, H.X.; Guo, W.J.; Wang, F.J. The main characteristics of Yalujiang Fault Zone and its significance. *Geol. Resour.* **2006**, *15*, 11–19. (In Chinese with English Abstract)
41. Xia, H.K.; Xu, D.M. Features of Yalujiang River Fault (south segment) activity and seismicity. *J. Seismol. Res.* **1993**, *16*, 391–400. (In Chinese with English Abstract)
42. Wang, Y.Z.; Wang, F.; Wu, L.; Shi, W.B.; Yang, L.Y. (U-Th)/He thermochronology of metallic ore deposits in the Liaodong Peninsula: Implications for orefield evolution in northeast China. *Ore Geol. Rev.* **2018**, *92*, 348–365. [[CrossRef](#)]
43. Wang, M.Z.; Ji, Z.J.; Liang, Q.G.; Jin, P.; Zhang, H.F.; Yang, Y.J. Ore-controlling structure characteristics and ore prospecting in Wulong gold deposit, Liaoning Province. *Geol. Miner. Resour. South China* **2011**, *27*, 191–196. (In Chinese with English Abstract)
44. Zhang, P.; Zhao, Y.; Kou, L.L.; Sha, D.M.; Bi, Z.W.; Yang, F.C. Zircon U-Pb Ages, Hf Isotopes and Geological Significance of Mesozoic Granites in Dandong Area, Liaodong Peninsula. *Earth Sci.—J. China Univ. Geosci.* **2019**, *44*, 3297–3313. (In Chinese with English Abstract)
45. Wei, J.H.; Qiu, X.P.; Guo, D.Z.; Tang, W.J. Geochemistry of ore fluids and Rb-Sr isotopic dating for the Wulong Gold Deposit in Liaoning, China. *Acta Geol. Sin.* **2004**, *78*, 1267–1274. (In Chinese with English Abstract)
46. Xiao, G.H.; Liu, T.X.; Zhang, G.X. Probing into the origin and mineralization model of Wulong Gold Deposit, Liaoning Province. *Gold* **2003**, *24*, 17–20. (In Chinese with English Abstract)
47. Wei, B.; Wang, C.Y.; Wang, Z.C.; Cheng, H.; Xia, X.P.; Tan, W. Mantle-derived gold scavenged by bismuth-(tellurium)-rich melts: Evidence from the mesozoic wulong gold deposit in the north china craton. *Ore Geol. Rev.* **2021**, *131*, 104047. [[CrossRef](#)]
48. Hou, K.J.; Li, Y.H.; Ye, T.R. In-situ U-Pb zircon dating laser ablation-multi iron counting-ICP-MS. *Miner. Depos.* **2009**, *28*, 481–492. (In Chinese with English Abstract)
49. Gao, J.F.; Zhou, M.F.; Lightfoot, P.C.; Wang, C.Y.; Qi, L.; Sun, M. Sulfide saturation and magma emplacement in the formation of the Permian Huangshandong Ni-Cu Sulfide Deposit, Xinjiang, Northwestern China. *Econ. Geol.* **2013**, *108*, 1833–1848. [[CrossRef](#)]
50. Zhu, Z.X.; Zhao, X.F.; Lin, Z.W.; Zhao, S.R. In Situ Trace Elements and Sulfur Isotope Analysis of Pyrite from Jinchiling Gold Deposit in the Jiaodong Region: Implications for Ore Genesis. *Earth Sci.—J. China Univ. Geosci.* **2020**, *45*, 945–959. (In Chinese with English Abstract)
51. Wang, J.P.; Liu, Z.J.; Liu, J.J.; Zeng, X.T.; Wang, K.X.; Liu, B.Z.; Wang, H.; Liu, C.H.; Zhang, F.F. Trace Element Compositions of Pyrite from the Shuangwang Gold Breccias, Western Qinling Orogen, China: Implications for Deep Ore Prediction. *J. Earth Sci.* **2018**, *29*, 564–572. [[CrossRef](#)]
52. Chen, W.T.; Zhou, M.F.; Li, X.; Gao, J.F.; Hou, K. In-situ LA-ICP-MS trace elemental analyses of magnetite: Cu-(Au, Fe) deposits in the Khetri copper belt in Rajasthan Province, NW India. *Ore Geol. Rev.* **2015**, *65*, 929–939. [[CrossRef](#)]
53. Liu, Y.S.; Hu, Z.C.; Gao, S.; Gunther, D.; Xu, J.; Gao, C.G.; Chen, H.H. In situ analysis of major and trace elements of anhydrous minerals by LA-ICP-MS without applying an internal standard. *Chem. Geol.* **2008**, *257*, 34–43. [[CrossRef](#)]
54. Tang, H.F.; Liu, C.Q.; Xie, G.G. Mass transfer and element mobility of rocks during regional metamorphism: A case study of metamorphosed pelites from the Shuangqiaoshan Group in Lushan. *Geol. Rev.* **2000**, *46*, 245–254. (In Chinese with English Abstract)
55. Klammer, D. Mass change during extreme acid-sulphate hydrothermal alteration of a Tertiary latite, Styria, Austria. *Chem. Geol.* **1997**, *141*, 33–48. [[CrossRef](#)]
56. O'Hara, K. Fluid flow and volume loss during mylonitization: An origin for phyllonite in an overthrust setting, North Carolina, U.S.A. *Tectonophysics* **1988**, *156*, 21–36. [[CrossRef](#)]
57. Zhang, Z.C.; Wang, Y.W.; Li, D.D.; Wang, W.; Li, S.H.; Qiu, J.Z.; Lai, C.; Li, X. Hydrothermal alteration and mineralization of Baiyun gold deposit in Liaodong Peninsula, North China Craton. *Geol. J.* **2020**, *56*, 2167–2191. [[CrossRef](#)]
58. Liu, J.B.; You, Z.D.; Zhong, Z.Q.; Li, L.R. Mass Balance Analysis of Mylonites in Ductile Shear Zone: A Case Study of Shewei Shear Zone in Qinling Group, Western Henan. *Earth Sci.—J. China Univ. Geosci.* **1993**, *18*, 757–814. (In Chinese with English Abstract)
59. Wu, S.Y.; Liu, S.S.; Hou, L. Elements migration during ore-forming process, Yata gold deposit, Southwestern Guizhou, China. *Sediment. Geol. Tethyan Geol.* **2021**, *41*, 585–598. (In Chinese with English Abstract)
60. Wu, D.H.; Xia, F.; Pan, J.Y.; Liu, G.Q.; Huang, G.L.; Liu, W.Q.; Wu, J.Y. Characteristics of hydrothermal alteration and material migration of Mianhuakeng uranium deposit in northern Guangdong Province. *Acta Petrol. Sin.* **2019**, *35*, 2745–2764. (In Chinese with English Abstract)
61. Qiu, K.F.; Yu, H.C.; Wu, M.Q.; Geng, J.Z.; Ge, X.K.; Taylor, R.D. Discrete Zr and REE mineralization of the Baerzhe rare-metal deposit, China. *Am. Mineral.* **2019**, *104*, 1487–1502. [[CrossRef](#)]

62. Yu, H.C.; Qiu, K.F.; Hetherington, C.J.; Chew, D.; Huang, Y.Q.; He, D.Y.; Geng, J.Z.; Xian, H.Y. Apatite as an alternative petrochronometer to trace the evolution of magmatic systems containing metamict zircon. *Contrib. Mineral. Petrol.* **2021**, *176*, 68. [[CrossRef](#)]
63. Li, H.D.; Pan, J.Y.; Xia, F.; Zhou, J.Y.; Liu, Y.; Zhong, F.J. Hydrothermal alteration and its geochemical characteristics of Lijialing deposit in Xiangshan uranium ore deposit. *Geoscience* **2016**, *30*, 555–566. (In Chinese with English Abstract)
64. Simon, G.; Huang, H.; Penner-Hahn, J.E.; Kesler, S.E.; Kao, L.S. Oxidation State of Gold and Arsenic in Gold-Bearing Arsenian Pyrite. *Am. Mineral.* **1999**, *84*, 1071–1079. [[CrossRef](#)]
65. Fleet, M.E.; Mumin, A.H. Gold-bearing arsenian pyrite and marcasite and arsenopyrite from Carlin Trend gold deposits and laboratory synthesis. *Am. Mineral.* **1997**, *82*, 182–193. [[CrossRef](#)]
66. Deditius, A.P.; Utsunomiya, S.; Renock, D.; Ewing, R.C.; Ramana, C.V.; Kesler, S.E. A Proposed New Type of Arsenian Pyrite, Composition, Nanostructure and Geological Significance. *Geochim. Cosmochim. Acta* **2008**, *72*, 2919–2933. [[CrossRef](#)]
67. Mikhlin, Y.; Romanchenko, A.; Likhatski, M.; Karacharov, A.; Erenburg, S.; Trubina, S. Understanding the Initial Stages of Precious Metals Precipitation: Nanoscale Metallic and Sulfidic Species of Gold and Silver on Pyrite Surfaces. *Ore Geol. Rev.* **2011**, *42*, 47–54. [[CrossRef](#)]
68. Goldfarb, R.J.; Mao, J.W.; Qiu, K.F.; Goryachev, N. The great Yanshanian metallogenic event of eastern Asia: Consequences from one hundred million years of plate margin geodynamics. *Gondwana Res.* **2021**, *100*, 223–250. [[CrossRef](#)]
69. Meng, L.Y. The silicide and metallogenetic in the hydrothermal deposit. *Chin. Sci. Bull.* **1998**, *43*, 575–579. (In Chinese with English Abstract)
70. Yang, L.Q.; Li, R.H.; Gao, X.; Qiu, K.F.; Zhang, L. A preliminary study of extreme enrichment of critical elements in the Jiaodong gold deposits, China. *Acta Petrol. Sin.* **2020**, *36*, 1285–1314. (In Chinese with English Abstract)
71. Wu, M.Q.; Samon, I.M.; Qiu, K.F.; Zhang, D.H. Multi-stage metasomatic Zr mineralization in the world-class Baerzhe Rare earth element-Nb-Zr-Be deposit. *Am. Mineral.* **2022**. [[CrossRef](#)]
72. Reich, M.; Kesler, S.E.; Utsunomiya, S.; Christopher, S.P.; Stephen, L.C.; Rodney, C.E. Solubility of gold in arsenian pyrite. *Geochim. Cosmochim. Acta* **2005**, *69*, 2781–2796. [[CrossRef](#)]
73. Li, W.; Cook, N.J.; Xie, G.Q.; Mao, J.W.; Ciobanu, C.L.; Li, J.W.; Zhang, Z.Y. Textures and trace element signatures of pyrite and arsenopyrite from the Gutaishan Au–Sb deposit, South China. *Miner. Depos.* **2019**, *54*, 591–610. [[CrossRef](#)]
74. Feng, J.Y.; Tang, L.; Santosh, M.; Zhang, S.T.; Sheng, Y.M.; Hu, X.K.; Wang, L. Genesis of hydrothermal gold mineralization in the Qianhe deposit, central China: Constraints from in situ sulphur isotope and trace elements of pyrite. *Geol. J.* **2021**, *56*, 3241–3256. [[CrossRef](#)]
75. Large, R.R.; Maslennikov, V.; Robert, F.; Danyushevsky, L.V.; Chang, Z. Multistage sedimentary and metamorphic origin of pyrite and gold in the giant Sukhoi Log deposit, Lena gold province, Russia. *Econ. Geol.* **2007**, *102*, 1232–1267. [[CrossRef](#)]
76. Large, R.R.; Danyushevsky, L.; Hollit, C. Gold and trace element zonation in pyrite using a laser imaging technique: Implications for the timing of gold in orogenic and Carlin-style sediment-hosted deposits. *Econ. Geol.* **2009**, *104*, 635–668. [[CrossRef](#)]
77. Qiu, K.F.; Yu, H.C.; Hetherington, C.; Huang, Y.Q.; Yang, T.; Deng, J. Tourmaline composition and boron isotope signature as a tracer of magmatic-hydrothermal processes. *Am. Mineral.* **2021**, *106*, 1033–1044. [[CrossRef](#)]
78. Wang, Y.; Qiu, K.F.; Müller, A.; Hou, Z.L.; Zhu, Z.H.; Yu, H.C. Machine learning prediction of quartz forming-environments. *J. Geophys. Res. Solid Earth* **2021**, *126*, e2021JB021925. [[CrossRef](#)]
79. Yu, H.C.; Qiu, K.F.; Simon, A.; Wang, D.; Mathur, R.; Wan, R.Q.; Jiang, X.Y.; Deng, J. Telescoped boiling and cooling mechanisms triggered hydrothermal stibnite precipitation: Insights from the world’s largest antimony deposit in Xikuangshan China. *Am. Mineral.* **2022**. [[CrossRef](#)]
80. Qiu, K.F.; Yu, H.C.; Deng, J.; McIntire, D.; Goldfarb, R.J. The giant Zaozigou orogenic Au–Sb deposit in West Qinling, China: Magmatic or metamorphic origin? *Miner. Depos.* **2020**, *55*, 345–362. [[CrossRef](#)]
81. Zhou, Z.K.; Yonezu, K.; Imai, A.; Tindell, T.; Li, H.; Gabo-Ratio, J.A. Trace elements mineral chemistry of sulfides from the Woxi Au–Sb–W deposit, Southern China. *Resour. Geol.* **2021**, *72*, e12279. [[CrossRef](#)]
82. Cook, N.J.; Chryssoulis, S.L. Concentrations of invisible gold in the common sulfides. *Can. Mineral.* **1990**, *28*, 1–16.
83. Zhang, P.; Kou, L.L.; Zhao, Y.; Bi, Z.W.; Sha, D.M.; Han, R.P.; Li, Z.M. Genesis of the wulong gold deposit, liaoning province, ne china: Constrains from noble gases, radiogenic and stable isotope studies. *Geosci. Front.* **2020**, *11*, 547–563. [[CrossRef](#)]
84. Zheng, B.; An, F.; Zhu, Y.F. Native bismuth found in Baogutu gold deposit and it’s geological significance. *Acta Petrol. Sin.* **2009**, *25*, 1426–1436. (In Chinese with English Abstract)
85. Deditius, A.P.; Reich, M.; Kesler, S.E.; Satoshi, U.; Stephen, L.C.; John, W.; Rodney, C.E. The coupled geochemistry of Au and As in pyrite from hydrothermal ore deposits. *Geochim. Cosmochim. Acta* **2014**, *140*, 644–670. [[CrossRef](#)]
86. Zhao, H.X.; Frimmel, H.E.; Jiang, S.Y.; Dai, B.Z. LA-ICP-MS trace element analysis of pyrite from the Xiaoqinling gold district, China: Implications for ore genesis. *Ore Geol. Rev.* **2011**, *43*, 142–153. [[CrossRef](#)]
87. Bralía, A.; Sabatini, G.; Troja, F. A reevaluation of the Co/Ni ratio in pyrite as geochemical tool in ore genesis problems. *Miner. Depos.* **1979**, *14*, 353–374. [[CrossRef](#)]
88. Loftus-Hills, G.; Solomon, M. Cobalt, nickel and selenium in sulfides as indicators of ore genesis. *Miner. Depos.* **1967**, *2*, 228–242. [[CrossRef](#)]
89. Wang, K.Y.; Qing, M.; Bian, H.Y.; Wan, D.; Sun, F.Y.; Liu, Z.H.; Ji, Z.J. The Geological Features and Geochemistry of Ore-Forming Fluids of Wulong Gold Deposit in Liaoning Province. *J. Jilin Univ.* **2010**, *40*, 557–564. (In Chinese with English Abstract)

90. Hayashi, K.I.; Ohmoto, H. Solubility of gold in NaCl- and H₂S- bearing aqueous solution at 250–350 °C. *Geochim. Cosmochim. Acta* **1991**, *55*, 2111–2126. [[CrossRef](#)]
91. Mills, S.E. Gold Deposit Genesis in the Jiaodong Gold District, Northeast China: Mineralogical and Geochemical Insights into Mesozoic Gold in an Archean Craton. Ph.D. Thesis, School of Geosciences, Monash University, Melbourne, Australia, 2013.
92. Fan, H.R.; Zhai, M.G.; Xie, Y.H.; Yang, J.H. Ore-forming fluids associated with granite-hosted gold mineralization at the Sanshandao deposit, Jiaodong gold province, China. *Miner. Depos.* **2003**, *38*, 739–750. [[CrossRef](#)]
93. Cox, S.F.; Sun, S.S.; Etheridge, M.A.; Wall, V.J.; Potter, T.F. Structural and geochemical controls on the development of turbidite-hosted gold quartz vein deposits, Wattle Gully mine, central Victoria, Australia. *Econ. Geol.* **1995**, *90*, 1722–1746. [[CrossRef](#)]
94. Zhen, M.H.; Gu, X.X.; Zhou, Y.F. An analysis of metallogenic physicochemical conditions and metallogenic processes of the Dongbeizhai micro-disseminated gold deposit in Sichuan province. *Miner. Depos.* **1990**, *9*, 129–140. (In Chinese with English Abstract)
95. Naden, J.; Shepherd, T.J. Role of methane and carbon dioxide in gold deposition. *Nature* **1989**, *342*, 793–795. [[CrossRef](#)]
96. Guo, L.N.; Liu, S.S.; Hou, L.; Wang, J.T.; Shi, M.F.; Zhang, Q.M.; Nie, F.; Yang, Y.F.; Peng, Z.M. Fluid Inclusion and H-O Isotope Geochemistry of the Phapong Gold Deposit, NW Laos: Implications for Fluid Source and Ore Genesis. *J. Earth Sci.* **2019**, *30*, 80–94. [[CrossRef](#)]
97. Bucher, K.; Stober, I. Interaction of Mantle Rocks with Crustal Fluids: Sagvandites of the Scandinavian Caledonides. *J. Earth Sci.* **2019**, *30*, 1084–1094. [[CrossRef](#)]
98. Wang, C.Y.; Wang, Q.S.; Sun, S.P.; Zhang, J. Temporal and Spatial Evolution of Ore-Forming Fluid and Metallogenic Mechanism in the Jinwozi Gold Deposit, Beishan Metallogenic Belt. *Earth Sci.—J. China Univ. Geosci.* **2018**, *43*, 3126–3140. (In Chinese with English Abstract)
99. Li, L.; Sun, F.Y.; Li, B.L.; Qian, Y.; Xu, Q.L. Ore-Forming Fluid Features and Genesis of Shabaosi Gold Deposit in Mohe County, Heilongjiang Province. *Earth Sci.—J. China Univ. Geosci.* **2015**, *40*, 1163–1176. (In Chinese with English Abstract)
100. Seward, T.M. Thio complexes of gold and the transport of gold in hydrothermal ore solutions. *Geochim. Cosmochim. Acta* **1973**, *37*, 379–399. [[CrossRef](#)]
101. Reich, M.; Deditius, A.; Chryssoulis, S.; Li, J.W.; Ma, C.Q.; Parada, M.A.; Mittermayr, F. Pyrite as a record of hydrothermal fluid evolution in a porphyry copper system: A SIMS/EMPA trace element study. *Geochim. Cosmochim. Acta* **2013**, *104*, 42–62. [[CrossRef](#)]
102. Groves, D.I.; Foster, R.P. Archaean lode gold deposits. In *Gold Metallogeny and Exploration*; Springer: Boston, MA, USA, 1991; pp. 63–103.
103. Xie, Y.L.; Yang, K.J.; Li, Y.X.; Li, G.M.; Qu, Y.W.; Dong, L. Mazhala Gold-Antimony Deposit in Southern Tibet: The Characteristics of Ore-Forming Fluids and The Origin of Gold and Antimony. *Earth Sci.—J. China Univ. Geosci.* **2019**, *44*, 1998–2016. (In Chinese with English Abstract)